ANNUAL REPORT ON

RADAR IMAGE ENHANCEMENT, FEATURE EXTRACTION AND MOTION COMPENSATION USING JOINT TIME-FREQUENCY TECHNIQUES

Submitted by

Professor Hao Ling

Department of Electrical and Computer Engineering
The University of Texas at Austin
Austin, TX 78712-1084

May 15, 2000

20000530 065

REPORT DOCUMENTATION PAGE

Public reporting burden for this collection of information is estimated to average 1 hour per response, including the time for reviewing instructions, searching existing data sources, gathering and maintaining the data needed, and completing and reviewing the collection of information. Send comments regarding this burden estimate or any other aspect of this collection of information, including suggestions for reducing this burden to Washington Headquarters Services, Directorate for Information Operations and Reports, 1215 Jefferson Davis Highway, Suite 1204, Arlington, VA 22202-4302, and to the Office of Management and Budget, Paperwork Reduction Project (0704-0188), Washington, DC 20503.

1. AGENCY USE ONLY *(Leave blank)*	2. REPORT DATE May 15, 2000	3. REPORT TYPE AND DATES COVERED Annual Report 15 April 99-14 April 00

4. TITLE AND SUBTITLE Annual Report on Radar Image Enhancement, Feature Extraction and Motion Compensation Using Joint Time-Frequency Techniques

5. FUNDING NUMBERS

Research Grant ONR
N00014-98-1-0615

6. AUTHOR(S)

Hao Ling

7. PERFORMING ORGANIZATION NAMES(S) AND ADDRESS(ES)

The University of Texas at Austin
Department of Electrical and Computer Engineering
Austin, TX 78712-1084

8. PERFORMING ORGANIZATION REPORT NUMBER

No. 2

9. SPONSORING / MONITORING AGENCY NAMES(S) AND ADDRESS(ES)

Office of Naval Research
Ballston Centre Tower One
800 North Quincy Street
Arlington, VA 22217-5660

Program Officer
William Miceli
ONR 313

10. SPONSORING / MONITORING AGENCY REPORT NUMBER

11. SUPPLEMENTARY NOTES

a. DISTRIBUTION / AVAILABILITY STATEMENT

Approved for Public Release
Distribution Unlimited

12. DISTRIBUTION CODE

13. ABSTRACT *(Maximum 200 words)*

This report summarizes the scientific progress on the research grant "Radar Image Enhancement, Feature Extraction, and Motion Compensation Using Joint Time-Frequency Techniques" during the period 15 April 1999-14 April 2000. Progress on processing of NATO TIRA and MERIC radar data, removal of image artifacts due to jet engine modulation, and three-dimensional motion detection and compensation is presented.

14. SUBJECT TERMS
Radar imaging, joint time-frequency techniques

15. NUMBER OF PAGES
62

16. PRICE CODE

17. SECURITY CLASSIFICATION OF REPORT Unclassified	18. SECURITY CLASSIFICATION OF THIS PAGE Unclassified	19. SECURITY CLASSIFICATION OF ABSTRACT Unclassified	20. LIMITATION OF ABSTRACT

ANNUAL REPORT ON

RADAR IMAGE ENHANCEMENT, FEATURE EXTRACTION AND MOTION COMPENSATION USING JOINT TIME-FREQUENCY TECHNIQUES

Submitted by

Professor Hao Ling

Department of Electrical and Computer Engineering
The University of Texas at Austin
Austin, TX 78712-1084

May 15, 2000

RADAR IMAGE ENHANCEMENT, FEATURE EXTRACTION AND MOTION COMPENSATION USING JOINT TIME-FREQUENCY TECHNIQUES

Project Starting Date: April 15, 1998

Reporting Period: April 15, 1999 – April 14, 2000

Principal Investigator: Professor Hao Ling
        (512) 471-1710
        ling@ece.utexas.edu

Graduate Students: Y. Wang, J. Li, H. Deng

Undergraduate Students: M. Andringa, D. Buhl

A. SCIENTIFIC OBJECTIVES: The objective of this research program is to devise innovative joint time-frequency (JTF) processing concepts for radar image enhancement and physics-based feature extraction. In particular, we shall investigate how JTF techniques can be utilized to enhance synthetic aperture radar (SAR) and inverse synthetic aperture radar (ISAR) imageries by removing artifacts due to uncompensated target motion, complex target scattering physics, articulating target components and clutter and propagation effects. Furthermore, we set out to re-interpret the extracted artifacts in a more meaningful feature space so that they can be utilized to enhance the performance of target identification algorithms. This research is leveraged against our previous JTF work under the Joint Services Electronics Program, as well as our state-of-the-art radar signature simulation capabilities. At the end of this program, we plan to develop a set of JTF-based radar image processing tools in the standard MATLAB environment, so that this work can be easily disseminated to the radar community.

B. SUMMARY OF RESULTS AND SIGNIFICANT ACCOMPLISHMENTS: During the past year, we have proceeded along two lines of research: (i) processing real radar data to test our JTF algorithms and to identify needed areas of research, (ii) developing new algorithms to address the problem areas identified. Along the first line, we have continued the processing of measured data from the NATO TIRA radar. By

applying the JTF motion compensation algorithm we had developed earlier, we have formed high-resolution ISAR images of several air targets and have compared the results to truth images generated using instrumented flight data and simulated images computed using the radar signature prediction code Xpatch. Through these comparisons, we have identified several problem areas for blind motion compensation due to the presence of either non-steady imaging plane or moving components on the target. These issues cannot be handled by the existing motion compensation algorithms and are being addressed in our theoretical algorithm development. We have also initiated an effort to process the NATO MERIC radar data set. Blind motion compensation is more challenging in this case, as the flight path of the aircraft is very close to the radar, which results in large variations in the aircraft's azimuth and elevation angles with respect to the radar.

Along the second line of research, we have focused on the two problem areas identified from processing of the TIRA data. First, we have developed and applied an adaptive JTF algorithm to remove jet engine modulation (JEM) lines caused by the scattering from the rotating engine blades of the aircraft. The algorithm distinguishes the slow body motion from the fast engine blade motion using the phase features in the JTF space. It is shown that JEM lines can be removed from the image to unveil the geometrical features of the aircraft. Second, we have initiated research to address the problem of blind motion compensation in the presence of non-steady imaging plane. This problem can be considered in the context of three-dimensional motion compensation and is much more challenging than conventional two-dimensional motion compensation. Toward this end, we have developed an algorithm to detect the presence of non-steady imaging plane during the imaging interval from raw radar data. This detection algorithm is based on a full three-dimensional motion model and compares the phase variation of the point scatterers in different range cells to detect the presence of three-dimensional motion. Furthermore, we have begun to investigate ways to form a focused image when the target undergoes such three-dimensional motion. We believe the three-dimensional motion compensation theories developed in this topic will be quite important, especially when imaging targets that exhibit more chaotic motions, such as ships on the ocean surface. The detailed descriptions of our progress are described below.

Processing of NATO TIRA Radar Data. Our research thrust during the first year of this project was to generate ISAR imagery from the NATO TIRA radar data using our previously developed adaptive JTF (AJTF) algorithm [1]. We have continued this activity into the second year by comparing the results against truth images generated using instrumented flight data and simulated images computed using the radar signature prediction code Xpatch. While the comparison among the images is quite good, we have identified several needed areas of research in ISAR-based target recognition. Fig. 1 shows both the correlation coefficient between the JTF and truth images and that between the JTF and Xpatch images versus azimuth look angle. From the two curves, we see that the JTF images agree very well with the truth images, indicating that blind motion compensation is a very feasible method for processing real-world radar data. The correlation coefficient between the JTF and Xpatch images is slightly lower than that between the measured images. In particular, two problem regions can be seen from this plot. First, in the region near nose-on (180 degrees in azimuth), the correlation coefficient is significantly lower. The reason is due to JEM lines in the measured data. This problem is further discussed in the next section and an algorithm to remove JEM lines is proposed. Second, at some angles around the broadside region (90 degrees in azimuth), the correlation coefficient is also low. In this case, both the associated JTF image and the truth image are both found to be of low quality. After further investigation, it is found that the image blurring is due to the non-steadiness of the imaging plane. This problem is also being further addressed in our research.
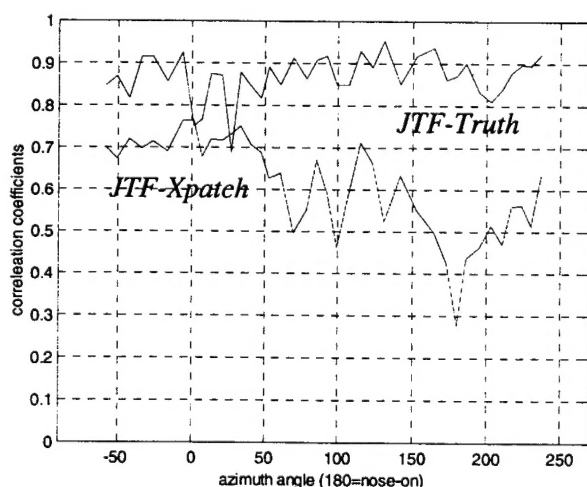

Fig. 1. Correlation coefficients between JTF and truth images, and between JTF and Xpatch images.

Removing Image Artifacts due to Jet Engine Modulation. Jet engine modulation (JEM) is a well-known phenomenon caused by the high-speed rotation of the aircraft engine. For imaging radar, the typical PRF is much slower than the engine rotation frequency. Thus the resulting ISAR image in the frontal region of an aircraft contains an aliased component along the cross range dimension, as shown by the TIRA image in Fig. 2(a). Such effect is difficult to predict accurately using simulation [2, 3]. Furthermore, JEM lines are noise-like and can corrupt the geometrical features of the target in the ISAR image. For ISAR-based target recognition, it would be useful to devise an algorithm to separate the JEM lines from the target image before the subsequent classification process. In the first year of this program, we successfully demonstrated the separation of the rotating blade contribution from the body image in helicopter data. However, JEM possesses new challenges due to the high rotational rate of the jet engine and additional electromagnetic propagation effect through the inlet duct. We have carried out JEM removal on TIRA data using the AJTF algorithm. The model we adopt assumes that the aircraft consists of a slowly rotating body with a constant rotational velocity Ω_b and a fast moving engine component with a different rotational velocity Ω_p. The received radar return as a function of dwell time can thus be written as:

$$
\begin{aligned}
E(t_D) = \sum_{k=1}^{N_b} A_k \exp[-j\frac{4\pi f}{c}(R(t_D) + x_k \cos(\Omega_b t_D) + y_k \sin(\Omega_b t_D)] \\
+ \sum_{k=N_b+1}^{N} A_k \exp[-j\frac{4\pi f}{c}(R(t_D) + x_k \cos(\Omega_p t_D) + y_k \sin(\Omega_p t_D)]
\end{aligned}
\tag{1}
$$

where N is the total number of point scatterers within one range cell, of which N_b are the body scatterers. Usually Ω_p is much greater than Ω_b. While the first term can be meaningfully mapped into the image plane of the target via the Fourier transform, the second term results in serious Doppler smearing across the cross range domain.

We can also utilize the AJTF technique to separate the fast moving part from the relatively slow moving body. For the component due to target body scattering, the Doppler frequency is

$$
f_D^b = \frac{4\pi f}{c}\Omega_b[y\cos(\Omega_b t_D) + x\sin(\Omega_b t_D)] \approx \frac{4\pi f}{c}\Omega_b(y + x\Omega_b t_D) \quad ,
\tag{2}
$$

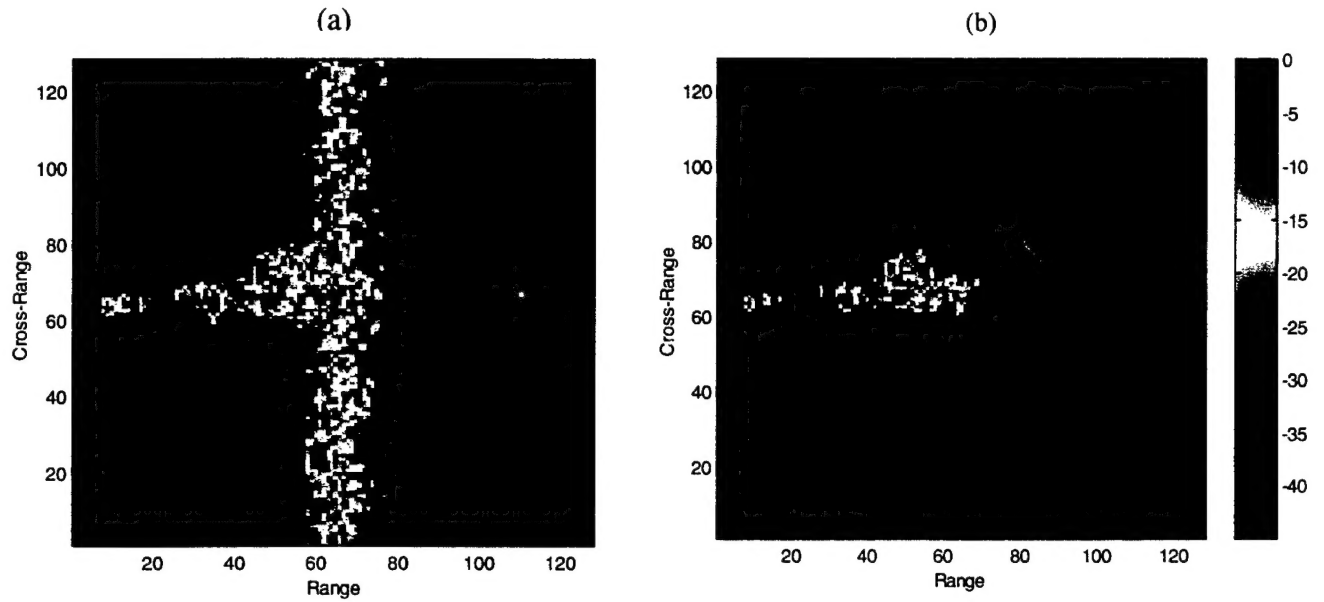while the Doppler frequency due to the fast rotating part is

Fig. 2. TIRA image from a frontal view. (a) Before JEM processing. (b) After JEM removal using the AJTF algorithm.

$$f_D^p = \frac{4\pi f}{c}\Omega_p[y\cos(\Omega_p t_D) + x\sin(\Omega_p t_D)] \tag{3}$$

We see that (2) is a linear function of dwell time while (3) is a sinusoidal function. If we parameterize the signal by basis functions that have linear Doppler frequency behavior as a function of dwell time, the two signals can be approximately separated by their displacement and slope parameters. We utilize the AJTF processing technique to carry out the parameterization. The signal component due to the target scattering is reconstructed by using all the bases with small displacement and small slope parameters. Fig. 2(b) shows the image after the JEM removal processing. Note that the body features are unveiled after the JEM removal. Fig. 3 shows the correlation between the synthetic images and the measured images from TIRA after JEM removal. We observe that the correlation coefficients in the JEM region are increased after we remove the JEM interference from the body. Further research is needed in this area to more definitively assess the effect of JEM removal. This will be carried out as more measured data
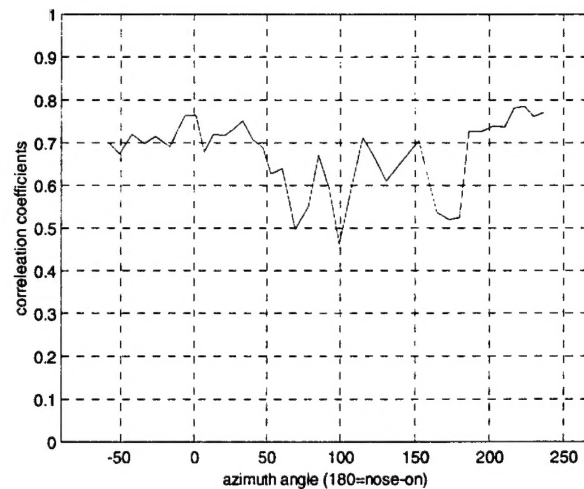
Fig. 3. Correlation between JTF and Xpatch images
after JEM removal.

become available. Furthermore, in the processing of the MERIC radar data, we have observed very clear indication of movement from a mechanically gimbaled antenna in the nose region of the aircraft. The algorithm will be adapted to study this issue.

Three-Dimensional Motion Detection Using JTF Algorithm. One basic assumption of existing motion compensation algorithms is that the target only undergoes motion in a two-dimensional plane during the dwell interval needed to form an image. From several independent examinations of measured ISAR data sets recently, it was reported that the presence of three-dimensional motion is quite detrimental to the formation of a well-focused image [5-7]. This is also consistent with our own findings from the TIRA data. For some image frames, we found that the motion compensated image and the associated truth images are both quite poor. An example image is shown in Fig. 4(a). When we examine the motion data from the aircraft instrument, we find that the aircraft motion is not confined to a two-dimensional plane during the imaging interval. Fig. 4(b) shows the plot of the elevation versus azimuth look angles of the aircraft from the radar. This curve should be linear if the motion is strictly two-dimensional, and in this case, there is clearly three-dimensional motion. In general, we will not be able to form a focused image using an existing motion compensation algorithm based on the two-dimensional motion
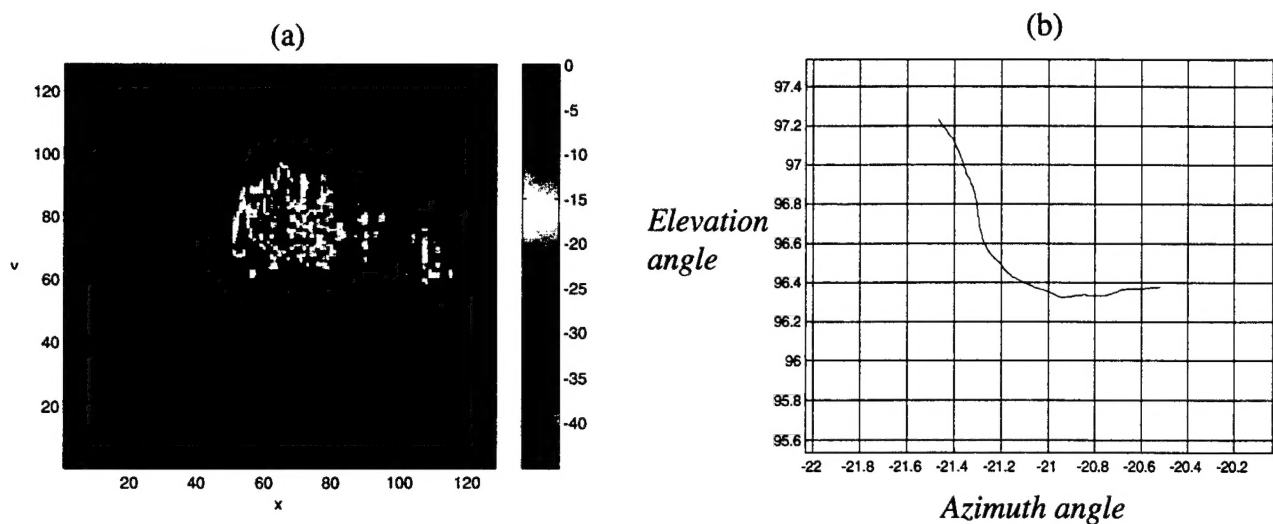
Fig. 4. Effect of non-steady imaging plane on image quality. (a) A poorly focused image. (b) The corresponding target motion from the instrumentation data.

assumption, since the assumed model is mismatched to the actual target motion. Our goal in this research is to develop a general motion compensation algorithm to handle targets with arbitrary three-dimensional motion. However, this problem is quite challenging. Instead, we first address a less ambitious problem of detecting the presence of three-dimensional motion from raw radar data. It is hoped that the solution here will be a stepping stone to the ultimate three-dimensional motion compensation problem.

Allowing for arbitrary three-dimensional motion in space, we consider the following model as a generalization of the two-dimensional motion model:

$$E(t_D) = \sum_{k=1}^{N} A_k \, exp[-j\frac{4\pi f_c}{c}(x_k + y_k\theta(t_D) + z_k\phi(t_D))] \tag{4}$$

where θ is the azimuth angle of the target with respect to the radar, and ϕ is the elevation angle. In (4), it is assumed that the translation motion has been removed and that the standard small-angle, small bandwidth approximations apply. This model reduces to the standard two-dimensional motion model when θ and ϕ are linearly related. Our approach to the three-dimensional motion detection problem is to utilize the AJTF algorithm to extract the phase behavior of the radar data at multiple range cells. It can be shown that when the target undergoes only two-dimensional motion during the dwell
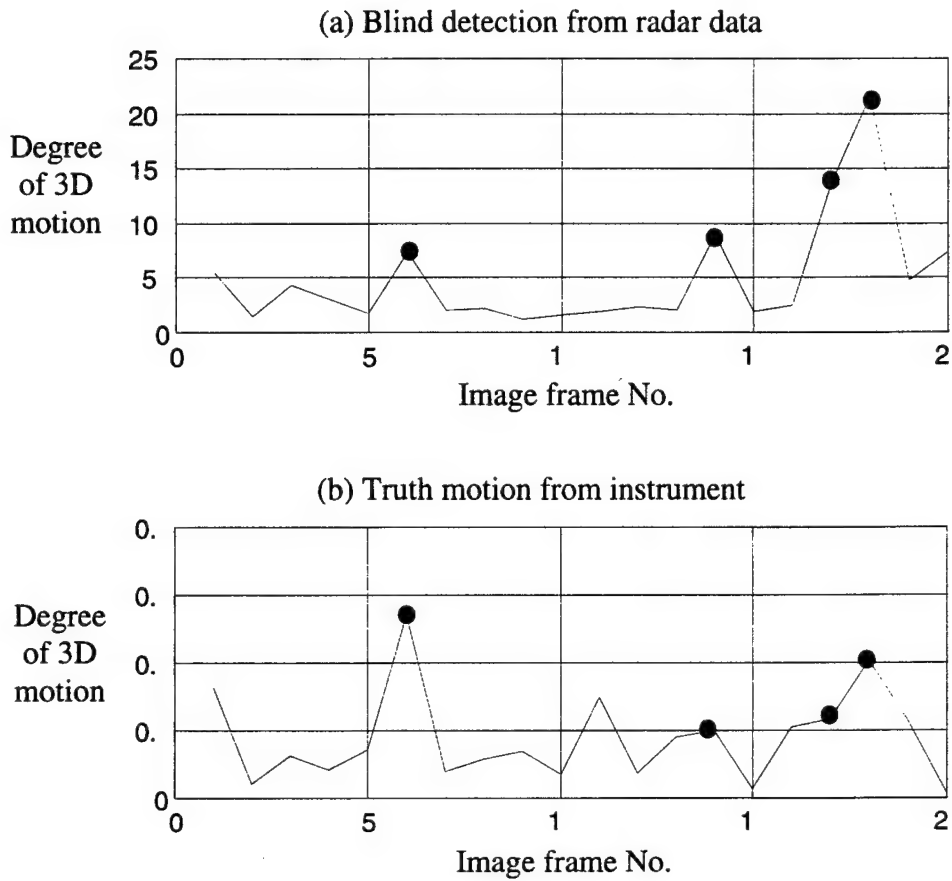
Fig. 5. Blind detection of three-dimensional motion from TIRA data. (a) Degree of three-dimensional motion over 20 image frames detected using the proposed algorithm. (b) Degree of three-dimensional motion measured from the instrument data.

duration, the relationship between the phase extracted from one range cell and that from another range cell should be linear. For three-dimensional motion, the relationship is in general nonlinear. Therefore, by examining the linearity of the phase relationships from different range cells, we can distinguish two-dimensional motion from three-dimensional motion. Fig. 5 shows our preliminary results from the TIRA data. Fig. 5(a) shows the degree of three-dimensional motion in the data for 20 different image frames, detected by applying our algorithm to the raw TIRA radar data. As a reference for comparison, Fig. 5(b) shows the degree of three-dimensional motion for the same 20 frames measured

using the instrumentation data. It can be seen that our algorithm correctly detects where significant three-dimensional motions exist. We are currently fine tuning the algorithm to achieve faster and more robust detection. We believe this detection algorithm could be quite useful for determining the "good" imaging intervals from which focused images can be more readily generated. For targets that exhibit very chaotic motions, such as ships on the ocean, finding such intervals of opportunity may be very critical for target recognition. Furthermore, we will try to devise algorithms for forming focused images even in the presence of significant three-dimensional motions.

Processing of NATO MERIC Radar Data. We have begun to process the MERIC radar data made available to us through the Naval Research Laboratory. Blind motion compensation is more challenging in this case, as the flight path of the aircraft is very close to the radar and the instrument data show more variations in azimuth and elevation angles during the flight of the aircraft. The task is further complicated by the lack of sufficient instrument data (some of the ARDS pod data have been heavily down-sampled and written into Microsoft Excel form in the MERIC data set). In addition, some of the radar data contain very strong colored noise in the background and considerable effort has been spent on denoising the data. Despite these difficulties, the final JTF image quality we have generated is fairly good. Fig. 6 shows the angular motion parameters of an aircraft for which the radar data are available. The aircraft undergoes an azimuth rotation of about 25 degrees during the 17.5-sec collection period. While there are 35,000 pulses of radar range profiles during this duration, only 18 samples of instrument data are available in the same duration. Consequently, no ground truthing was possible due to the lack of sufficient instrument data. To validate our results, we have generated the Xpatch prediction using a CAD model purchased from viewpoint.com. It is however not the exact model for the aircraft used in the measurement. The model was first converted into an Xpatch-compatible format. It was then edited to remove the landing gear and bomb loads under the wings, as well as to seal up the open seams in the model. Some preliminary comparison results are presented in Fig. 7. Figs. 7(a) and 7(b) show respectively the JTF motion compensated image and the Xpatch predicted image near

point P of Fig. 6 in the flight path. The agreement between the MERIC image and the Xpatch simulated image is fairly good, considering the uncertainties in the CAD model.
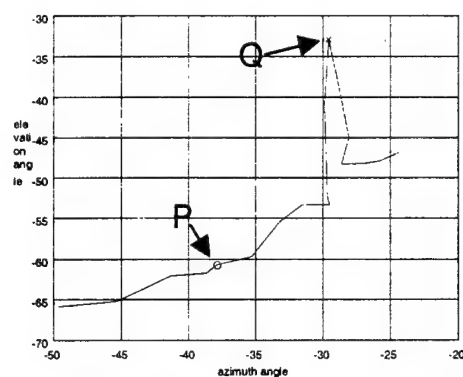

Fig. 6. Azimuth versus elevation angles of the aircraft with respect to the radar during the flight path.
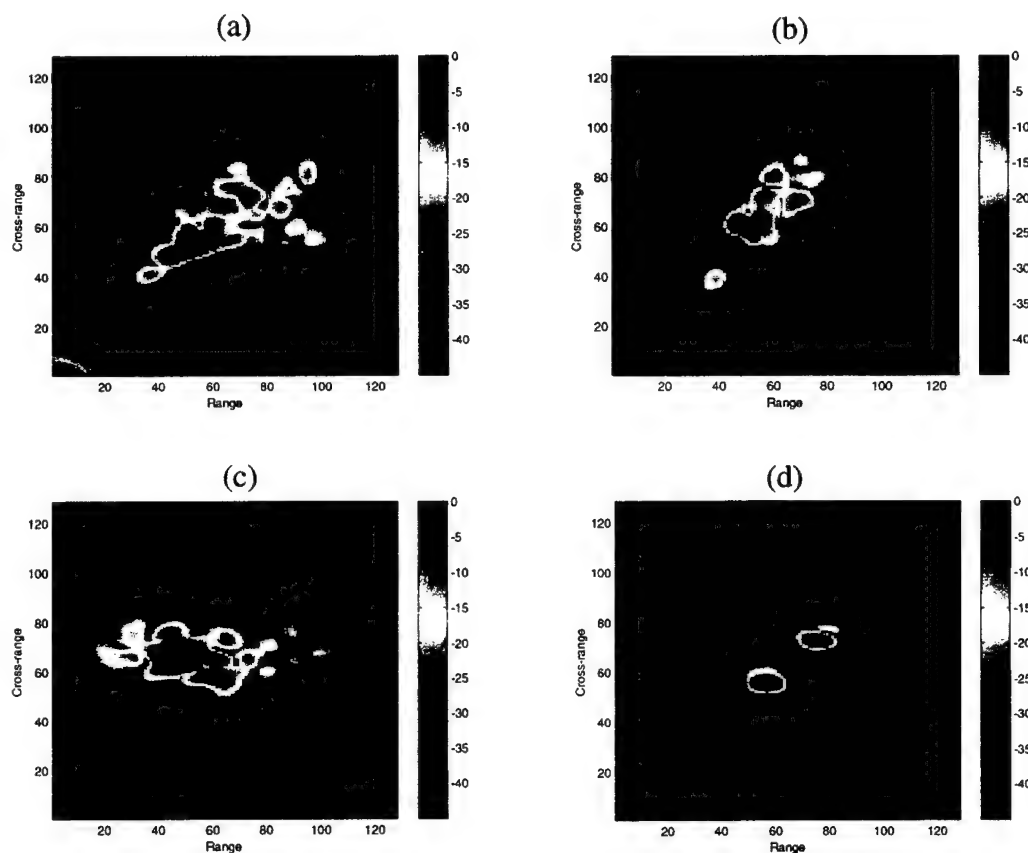

Fig. 7. Comparison of the MERIC image to Xpatch simulation. (a) JTF motion compensated image at point P. (b) Xpatch simulated image at point P. (c) JTF motion compensated image at point Q. (b) Xpatch simulated image at point Q.

Figs. 7(c) and 7(d) show respectively the JTF motion compensated image and the Xpatch predicted image near point Q of Fig. 6 in the flight path. It is clear that the agreement is quite poor in this case. The blind image formation is quite challenging during this particular portion of the flight. Furthermore, we are not certain of the exact imaging plane for the simulation due to the sparseness of instrument data. We plan to continue work on this data set and hope to eventually use the data set to further our investigation on three-dimensional motion detection and compensation. In addition, an interesting phenomenon was observed from the motion compensated image of a second aircraft. The formed images show Doppler smearing near the nose region. After some research on this aircraft, we have determined that it is very likely due to movement from a mechanically scanned antenna in the nose cone of the aircraft. We plan to examine this topic in more detail.

C. FOLLOW-UP STATEMENT:

During the coming year, our research effort will be devoted to developing new algorithms to attack the research problems we have identified through our work in measurement data processing. The research areas include: (i) three-dimensional motion detection and three-dimensional motion compensation, and (ii) image formation and feature extraction of targets with multiple moving parts. We believe these two problems are of fundamental importance in ISAR imaging, as the current state-of-the-art ISAR algorithms are limited by the two-dimensional motion and rigid body assumptions. For real-world data that involve more complex motions, such as ships with arbitrary motion and moving ocean surface, a more generalized motion compensation framework will be highly desirable. In addition to algorithm development, we will also continue our effort to process new radar data as they become available to us. Our work in the MERIC data will continue, and we will more closely examine the ship data from the Navy small craft ATR program. The measurement data processing enables us to identify relevant problems that can feed back into our theoretical investigation. Furthermore, the processed data sets provide us with a well-understood database, from which we can test our new algorithms.

D. REFERENCES:

1. Y. Wang, H. Ling and V. C. Chen, "ISAR motion compensation via adaptive joint time-frequency technique," *IEEE Trans. Aerospace Electron. Syst.*, vol. 34, pp.670-677, Apr. 1998.

2. R. Bhalla, H. Ling, S. W. Lee and D. J. Andersh, "Dynamic simulation of Doppler spectra of targets with rotating parts," *Microwave Optical Tech. Lett.*, vol. 7, pp. 840-842, December 1994.

3. R. Bhalla and H. Ling, "A fast algorithm for simulating Doppler spectra of targets with rotating parts using the shooting and bouncing ray technique," *IEEE Trans. Antennas Propagat.*, vol. AP-46, pp. 1389-1391, September 1998.

4. Y. Wang, H. Ling and V. C. Chen, "Application of adaptive joint time-frequency processing to ISAR image enhancement and Doppler feature extraction for targets with rotating parts," SPIE 43rd Annual Meeting, Radar Processing, Technology, and Applications, vol. 3462, pp. 156-163, San Diego, CA, July 1998.

5. V.C. Chen and W. J. Miceli, "Analysis of rotation effects on ISAR imaging based on TIRA radar and ARDS data," NATO Sensors and Electronics Technology Symposium on High-Resolution Radar Techniques, Granada, Spain, March 1999.

6. U. Uschkerat, "ISAR imaging using the point scatterer model and real target motion," NATO Sensors and Electronics Technology Symposium on High-Resolution Radar Techniques, Granada, Spain, March 1999.

7. W. Rihaczek and S. J. Hershkowitz, "Choosing imaging intervals for identification of small ships," SPIE Proc. on Radar Processing, vol. 3810, Denver, CO, July 1999.

E. PUBLICATIONS:

I. LIST OF JOURNAL ARTICLES (ONR supported in whole or in part)

8. Y. Wang and H. Ling, "Adaptive ISAR image construction from unevenly undersampled data," *IEEE Trans. Antennas Propagat.*, vol. AP-48, pp. 329-331, February 2000.

9. H. Deng and H. Ling, "Clutter reduction for synthetic aperture radar imagery based on adaptive wavelet packet transform," *Progress in Electromag. Research*, vol. 29, pp. 1-23, March 2000.

II. LIST OF CONFERENCE PROCEEDINGS (ONR supported in whole or in part)

10. H. Deng and H. Ling, "Clutter reduction for synthetic aperture radar images using adaptive wavelet packet transform," International IEEE AP-S Symposium, pp. 1780-1783, Orlando, FL, July 1999.

11. R. Bhalla, H. Ling and J. Schmitz, "Dynamic signature simulation using the shooting and bouncing ray technique," URSI National Radio Science Meeting, p. 272, Orlando, FL, July 1999.

12. J. Li, Y. Wang, R. Bhalla, H. Ling and V. C. Chen, "Comparison of high-resolution ISAR imageries from measurement data and synthetic signatures," SPIE 44th Annual Meeting, Radar Processing, Technology, and Applications, vol. 3810, pp. 170-179, Denver, CO, July 1999.

13. H. Ling and J. Li, "Application of adaptive joint time-frequency processing to ISAR image formation," submitted for presentation at the 10th IEEE Workshop on Statistical Signal and Array Processing, Pennsylvania, August 2000.

III. LIST OF RELATED PRESENTATIONS

14. "Fast postprocessing algorithms for fast CEM solvers," 1999 Electromagnetics Code Consortium Annual Meeting, Hughes Research Laboratory, Malibu, California, Apr. 20, 1999.

15. "Evaluation of Apatch – a platform radiation code based on the shooting and bouncing ray technique," Navy DD-21 Program Electromagnetic Software Evaluation Meeting, Navy SPAWAR System Center, San Diego, California, September 27, 1999.

IV. LIST OF THESES AND DISSERTATIONS

Ph.D.
Y. Wang, "Radar signature prediction and feature extraction using advanced signal processing techniques," August 1999.

V. CONTRACTS AND GRANTS

H. Ling, "MURI center for computational electromagnetics research," Air Force Office of Scientific Research (via Univ. of Illinois), December 15, 1995 - December 14, 2000.

H. Ling, "Application of model-based signal processing methods to computational electromagnetics simulators," Office of Naval Research, December 1, 1997 - November 30, 2000.

H. Ling, "Radar image enhancement, feature extraction and motion compensation using joint time-frequency techniques," Office of Naval Research, April 15, 1998 - April 14, 2001.

H. Ling, "Electromagnetic scattering from periodic surfaces," Lockheed Martin Corporate Grant, November 15, 1998 - December 31, 1999.

D. T. Jaffe and H. Ling, "High index grisms for mid-infrared spectroscopy," NASA, June 1, 1999 – May 31, 2001.

G. Xu, H. Ling and H. D. Foltz, "Development of wideband vector channel models and testbed for 3rd generation wireless mobile systems," Texas Advanced Technology Program, January 1, 2000 - December 31, 2001.

F. INTERACTIONS/COLLABORATIONS WITH NAVY SCIENTISTS:

Our key collaborator in this program is Dr. Victor Chen of Naval Research Laboratory. Our interactions with Dr. Chen include the exchange of data and algorithms. We have also co-authored a number of publications on JTF processing. It is expected that our close collaboration will continue since it provides an excellent way for us to stay informed of the problems of interest to the Navy and for us to quickly disseminate our research to the Navy labs.

The PI participated in an electromagnetic software evaluation meeting held at SPAWAR for the Navy's DD-21 program on Sept. 27, 1999. The PI presented an evaluation of the high-frequency code Apatch for characterizing antenna-platform interactions during the meeting. He also had technical discussions with Dr. William Pala of NRL, Dr. Jeffrey Ho of SPAWAR, and other scientists from government, industry and academic organizations.

G. NEW DISCOVERIES, INVENTIONS, OR PATENT DISCLOSURES:
None.

H. HONORS AND AWARDS:

Dr. Ling has been elected to IEEE Fellow for 1999 for his "contribution to the development of radar signature prediction and feature extraction techniques."

APPENDIX

Publications Supported by ONR

Research Grant N00014-98-1-0615

Adaptive ISAR Image Construction from Nonuniformly Undersampled Data

Yuanxun Wang and Hao Ling

Abstract—An adaptive approach is proposed to construct ISAR images from nonuniformly undersampled data in the angular domain. The algorithm uses an adaptive scattering feature extraction engine in place of the Fourier transform in the image construction procedure. The algorithm entails searching and extracting out individual target scattering features one at a time in an iterative fashion. The interference between different target scattering features is thus avoided and a clean ISAR image without the aliasing effect can be obtained. The algorithm is verified by constructing the ISAR image from the chamber measurement data of the model VFY-218 airplane.

Index Terms—Image reconstruction, synthetic aperture radar.

I. INTRODUCTION

Constructing an inverse synthetic aperture radar (ISAR) image of a target requires data collection in both the frequency and angular dimensions. If the data are uniformly sampled and the sampling rate is dense enough, an ISAR image can be obtained by using a two-dimensional (2-D) fast Fourier transform (FFT) algorithm [1]. In this paper, we address the case when the angular data are nonuniformly undersampled. This scenario may arise in real-world data collection when the target is fast maneuvering with respect to the radar pulse repetition interval so that the angular look on the target by the radar is not dense enough to satisfy the Nyquist sampling rate. We propose an algorithm to overcome the aliasing effect in the cross-range dimension and construct ISAR images from seriously undersampled data. The algorithm uses an adaptive scattering feature extraction engine in place of the Fourier transform in the image construction process. The original concept of adaptive feature extraction was proposed in [2] and [3]. It has been applied to ISAR image processing in the joint time–frequency space for resonant scattering mechanism extraction [4], target motion compensation [5], and Doppler interference removal [6]. In contrast to the Fourier transform, where the signal is projected to all the image-domain bases simultaneously, the adaptive algorithm searches and extracts the individual target scattering features one at a time in an iterative fashion. When applied to the present problem, the aliasing error caused by the interference between different target scattering features can be avoided. Therefore, after all the main features are extracted, they can be displayed in the ISAR image plane without the aliasing effect. We verify this algorithm by constructing the ISAR image using the chamber measurement data of the model VFY-218 airplane [7]. It is found that a reasonable ISAR image can be constructed from seriously undersampled data.

II. ADAPTIVE FEATURE EXTRACTION (AFE) ALGORITHM

In standard ISAR image construction, the target is assumed to be a collection of point scattering centers. Under the small-angle approx-

imation, the scattered field from the target observed as a function of frequency and angle can be written as

$$E(f, \theta) = \sum_{i=1}^{N} O(x_i, y_i) e^{-2jkx_i \cos\theta - 2jky_i \sin\theta}$$

$$\cong \sum_{i=1}^{N} O(x_i, y_i) e^{-2jkx_i - 2jk_c \theta y_i} \qquad (1)$$

where $O(x_i, y_i)$ is the amplitude of the ith scattering center, k is the free-space wave number, and k_c corresponds to the wave number at the center frequency. x_i and y_i denote the down range and cross-range dimensions, respectively. We assume that the sampling in frequency is uniformly spaced and dense enough to satisfy the Nyquist criterion since it is completely controlled by the radar. Thus, the range profile versus angle data can be generated from the frequency-aspect data by applying a one-dimensional (1-D) Fourier transform along the frequency dimension. We shall denote the result as $R(x, \theta)$

$$R(x, \theta) = \sum_{i=1}^{N} O(x_i, y_i) S_x(x - x_i) e^{-2jk_c y_i \theta}. \qquad (2)$$

In the above expression, $S_x(x - x_i)$ is the down-range point spread function due to the finite-length frequency domain data. Similarly, the cross-range information can also be obtained from angular data via a 1-D Fourier transform of $R(x, \theta)$ along the angular dimension. The resulting image $I(x, y)$ is

$$I(x, y) = \int R(x, \theta) e^{2jk_c y\theta} \, d\theta$$

$$= \sum_{i=1}^{N} O(x_i, y_i) S_x(x - x_i) \int e^{2jk_c \theta(y - y_i)} \, d\theta$$

$$= \sum_{i=1}^{N} O(x_i, y_i) S_x(x - x_i) S_y(y - y_i) \qquad (3a)$$

where

$$S_y(y - y_i) = \int e^{2jk_c \theta(y - y_i)} \, d\theta \qquad (3b)$$

is the cross-range point spread function due to the finite-length angular domain data. If the data are sampled densely enough such that the numerical integration can be carried out accurately, the point-spread function S_y should be a well-localized function with its peak at y_i, while rapidly decaying away from the peak. The resulting image $I(x, y)$ will be a clean image with good indication of the amplitudes and positions of the target point scattering features. However, when the data are undersampled, the numerical integration in (3b) will result in large aliasing error that shows up as high sidelobes in S_y. Consequently, the constructed image will contain strong interference between the scattering features. This effect can be interpreted as the loss of orthogonality of the Fourier bases under the undersampled condition.

In the proposed approach, we use an adaptive feature extraction algorithm in place of the Fourier processing. Instead of projecting the signal onto all the exponential bases simultaneously, we search out the strongest point scattering feature in the cross-range domain and remove it from the original signal. Then the search is repeated for the remainder signal and the point-scattering features are extracted one at a time until the energy of the residue signal is smaller than a preset threshold. The search procedure is carried out by calculating the integral in (3b) for all points in cross range but saving only the maximum value and position, i.e.,

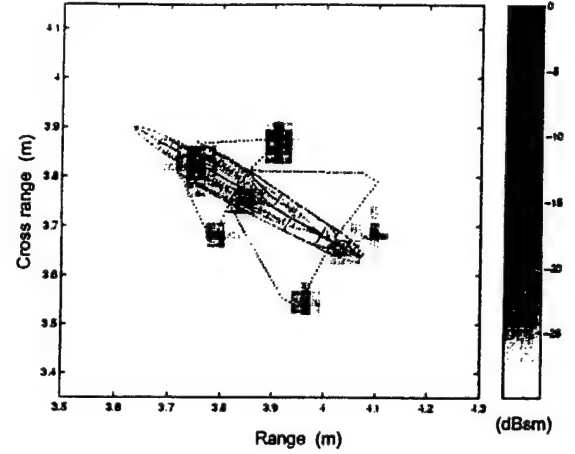$$[B_p, y_p] = \max_{y_p} [I_p(x, y)] \qquad (4)$$

Fig. 1. The ISAR image constructed at 30° azimuth from the original data using FFT.
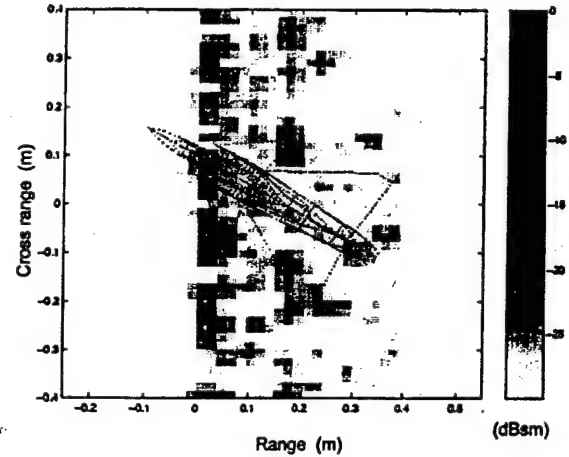

Fig. 2. The ISAR image constructed at 30° azimuth from randomly undersampled data using Fourier transform.

where p denotes the stage of the iterative procedure. The remainder signal is produced by subtracting out the pth feature

$$R_{p+1}(x, \theta) = R_p(x, \theta) - B_p e^{-2jk_c y_p \theta}. \qquad (5)$$

The convergence of the above procedure is guaranteed and the mathematical proof is given in [2]. The advantage of such an iterative procedure is that each time we extract out the strongest feature, we also eliminate its interference on the other features. It should be noted that nonuniform sampling is a prerequisite to ensure that there is no ambiguity in the strongest features since uniformly undersampled data will result in multiple positions of the strongest features. For simplicity, the algorithm is repeated for each range cell of the image. A 2-D algorithm in frequency and aspect can also be developed, if the search is carried out for both the range and cross-range parameters. After all the features are extracted out, we can construct an ISAR image using the amplitudes and positions of the point scatterers.

III. RESULTS AND DISCUSSION

To examine the applicability of the algorithm on real target scattering data, we reconstruct the radar image of a model (1 : 30 scale) VFY-218 airplane using undersampled chamber measurement data [7]. The measurement data consist of an aspect window from 10° to 50° and a frequency range from 8 to 16 GHz. To construct an ISAR image, we first
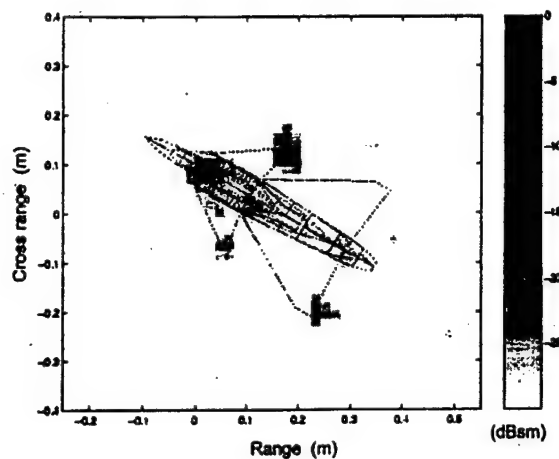
Fig. 3. The ISAR image constructed at 30° azimuth from randomly undersampled data using the AFE algorithm.

polar reformat the frequency-aspect data to the (K_x, K_y) space. The reformatted data consist of 401 samples in K_x and 438 samples in K_y. The ISAR image is first generated by fast Fourier transform (FFT) and shown with the airplane overlay in Fig. 1. The point-scattering features can clearly be seen. Next, we test our algorithm by generating an undersampled data set in K_y. This is approximately the same as undersampling in angle. (Note that for full size targets, this approximation gets better.) The Nyquist sampling rate requires about 36 sampling points in K_y and we randomly select only 24 out of the 438 points. The maximum sampling interval used is about four times the size of the Nyquist sampling interval. Therefore, serious aliasing will occur if the Fourier transform algorithm is used, as shown by the ISAR image displayed in Fig. 2. All the features are overlapped with sidelobe noise such that the point scattering features on the airplane can no longer be distinguished. Next, we apply the adaptive feature extraction (AFE) algorithm to each range cell of the image. The image is reconstructed and shown in Fig. 3. Comparing Fig. 3 with Fig. 1, we can see the main features of the airplane in Fig. 3 are all well reconstructed in Fig. 1. We do observe some noisy spots outside the target at the lower dynamic ranges in Fig. 3. This low-level noise occurs at about 25 dB down from the key features and presents a dynamic range limitation of the present AFE algorithm. The algorithm has also been tested on measured data from in-flight targets with good success.

REFERENCES

[1] D. A. Ausherman, A. Kozma, J. L. Walker, H. M. Jones, and E. C. Poggio, "Developments in radar imaging," *IEEE Trans. Aerosp. Electron. Syst.*, vol. AES-20, pp. 363–400, July 1984.

[2] S. Qian and D. Chen, "Signal regression using adaptive normalized Gaussian functions," *Signal Processing*, vol. 36, pp. 1–11, Mar. 1994.

[3] S. G. Mallat and Z. Zhang, "Matching pursuits with time-frequency dictionaries," *IEEE Trans. Signal Processing*, vol. 41, pp. 3397–3415, Dec. 1993.

[4] L. C. Trintinalia and H. Ling, "Joint time-frequency ISAR using adaptive processing," *IEEE Trans. Antennas Propagat*, vol. 45, pp. 221–227, Feb. 1997.

[5] Y. Wang, H. Ling, and V. C. Chen, "ISAR motion compensation via adaptive joint time-frequency techniques," *IEEE Trans. Aerosp. Electron Syst.*, vol. 34, pp. 670–677, Apr. 1998.

[6] ——, "Application of adaptive joint time-frequency processing to ISAR image enhancement and Doppler feature extraction for targets with rotating parts," in *SPIE Proc. Radar Processing, Technol. Applicat.* San Diego, CA, July 1998, vol. 3462.

[7] "Radar cross section measurement data of the VFY 218 configuration," Naval Air Warfare Center, China Lake, CA, Tech. Rep. NAWCWPNS TM-7621, Jan. 1994.

CLUTTER REDUCTION FOR SYNTHETIC APERTURE RADAR IMAGERY BASED ON ADAPTIVE WAVELET PACKET TRANSFORM

H. Deng and H. Ling

Department of Electrical and Computer Engineering
The University of Texas at Austin
Austin, TX 78712–1084

Abstract–An adaptive wavelet packet transform (AWPT) algorithm is proposed to process synthetic aperture radar (SAR) imagery and remove background clutters from target images. Since target features are more efficiently represented using the wavelet packet bases, higher signal-to-clutter ratios (SCR) can be achieved in the wavelet transform domain. Consequently, clutters can be more effectively separated from the desired target features in the transform domain than in the original SAR domain. The processed results based on the MSTAR data set demonstrate the effectiveness of this algorithm for SAR clutter reduction.

1. INTRODUCTION

Synthetic aperture radar (SAR) images of ground targets after the
focusing process generally consist of target images and clutters from
background scattering [1]. The clutter signal is undesirable since it in-
terferes with the actual target features in automatic target recognition
(ATR) applications, and has to be removed before ATR processing.
The traditional way to suppress clutter is to choose a threshold using
CFAR that is based on the standard deviation and mean value of the
clutter, and the threshold is applied to the SAR image chip to remove
the clutter directly [2, 3]. However, this approach assumes that the
target signal-to-clutter ratio (SCR) is large enough. If this assumption
is not true, this approach results in either target feature loss or large
clutter residues. In this work, we investigate the use of orthogonal basis
transformation to increase the SCR for more effective clutter removal.
More specifically, our approach is to find the best wavelet packet basis
to represent a SAR image using the adaptive wavelet packet transform
(AWPT) [4–9].
    Wavelet packet basis is a generalization of the conventional wavelet
basis. It retains the multi-resolution property of the conventional
wavelet basis while abandoning the rigid constant-Q structure in the
decomposition. Wavelet packets have been applied to image compres-
sion [7] and moment matrix sparsification [9] with good success. Theo-
retically they include regular pulse basis, FFT basis, short-time Fourier
transform (STFT) basis, as well as conventional wavelet basis. In this
application, we transform the SAR image into the wavelet packet basis
to maximize the signal-clutter-ratio in the transform domain. Since
a typical target image usually consists of point scatterers and more
diffused region features, the multi-scaled wavelet basis is well suited to
focus the target image. Clutter in the images, on the other hand, is sta-
tistically uncorrelated (or weakly correlated) from pixel to pixel, and
the transformed clutter image under the same set of bases remains un-
focused [8, 10, 11]. Therefore, we expect that the SCR can be increased
by transforming the original image with an appropriately chosen set of
wavelet packet basis. To determine the best basis for a SAR image, we
implement the AWPT algorithm to search for the best wavelet packet

basis based on a cost function that describes how well the target signal is focused in the transform domain. Because clutter in a SAR image is usually not strictly white, we apply a frequency-dependent threshold to the transformed image. We then inverse-transform the thresheld image in the wavelet packet basis domain back to the SAR domain to obtain a de-cluttered target image.

This paper is organized as follows. In Section 2, we introduce the basic concept of wavelet packet basis. In Section 3, we discuss problem formulation and the algorithm for SAR clutter rejection based on the adaptive wavelet packet transform. In Section 4, we present the test results of the algorithm using the MSTAR data set [12]. In Section 5, we draw some conclusions from this work.

2. WAVELET PACKET BASIS FOR SIGNAL REPRESENTATION

A wavelet packet basis function can be expressed in the space domain as:

$$\varphi_{j,k}^n(x) = 2^{-j/2}\psi_n(2^{-j}x - k), \ k \in Z, \ j \in Z, \ n \in Z_+ \tag{1}$$

where k, j, and n denote the space shift, scale, and modulation index, respectively. The function ψ_n can be generated from the decompositions of both the scaling function and mother wavelet function using the "two-scale equation" [4, 5]. The parameter choice of a wavelet packet basis is not unique for a complete and orthogonal decomposition of a signal in L^2 space. For a wavelet packet basis function $\varphi_{j,k}^n$, we define its dyadic interval $I_{j,n} \subset \Re$ in the frequency domain as [4, 9]:

$$I_{j,n} = \left[2^{-j}n, \ 2^{-j}(n+1)\right) \tag{2}$$

For the complete and orthogonal wavelet basis functions $\{\varphi_j^n\}$ chosen to represent a signal in L^2 space, their dyadic intervals should be disjoint and cover the entire signal bandwidth, i.e.,

$$\bigcap_{j,n} I_{j,n} = [\varnothing] \tag{3}$$

and

$$\bigcup_{j,n} I_{j,n} = [0,1) \tag{4}$$

Therefore, the wavelet packet basis function φ_j^n can be interpreted as a modulated wavelet with a central frequency of $2^{-j}(n + 1/2)$ and a normalized bandwidth of 2^{-j}.

For two-dimension image decomposition, the 2-D wavelet packet basis function can be configured from two 1-D wavelet packet basis functions as follows:

$$U_{p,q}^j(m, n) = \psi_{j,m}^p \psi_{j,n}^q \tag{5}$$

In (5), we restrict the scales of the two 1-D basis functions to be the same. This guarantees the basis functions will be of the same size in the horizontal and vertical directions, and remove the inter-scale coupling terms in the transformed image. For a complete and orthogonal decomposition, the two 1-D basis functions in (5) must also meet the requirements in (3) and (4).

Assuming that the original image in the spatial (SAR) domain is $\{s(m, n), 0 \leq m, n < N\}$, we define a set of complete and orthonormal 2-D wavelet packet basis functions:

$$\{U_{p,q}^j(k, l) \ 0 \leq j < J, \ 0 \leq p, \ q < 2^j, \ 0 \leq k, \ l < N2^{-j}\} \tag{6}$$

where j denotes the scale, $J = \log_2(N)$, p and q are the frequency modulation indices, and k, l are the position indices. The decomposition coefficients of the image $s(m, n)$ using the wavelet packet basis (6) are:

$$\widetilde{S}_{p,q}^j(k, l) = \sum_m \sum_n s(m, n) U_{p,q}^j(k - 2^j m, l - 2^j n) \tag{7}$$

With the image extended to be periodic in the spatial domain, the total number of coefficients is exactly N^2 through the transform in (7). For convenience, we refer to the coefficients as simply a matrix $\{\widetilde{S}(m, n), 1 \leq m, n \leq N\}$ without explicit indication of j, p and q.

Given a SAR image $s(m, n)$, we set out to find the best wavelet packet basis to maximize the SCR in transform domain. In the other words, we try to make the transformed coefficient matrix $\{\widetilde{S}(m, n), 1 \leq m, n \leq N\}$ as sparse as possible.

3. SAR IMAGE CLUTTER REDUCTION USING ADAPTIVE WAVELET PACKET TRANSFORM

3.1 Statistical Signal Model

We assume that a focused SAR image in spatial domain is:

$$\{s(m, n),\ 0 \le m,\, n < N\} \tag{8}$$

Ignoring additive noise and possible multiplicative speckle noise in the image, we consider a SAR image that consists of only the target image and clutters generated from the background scattering [15]. Basically the target image and the clutters are non-overlapping in a SAR image, therefore there is:

$$s(m, n) = \begin{cases} t(m, n), & (m, n) \text{ in target area} \\ c(m, n), & (m, n) \text{ in clutter area} \end{cases} \quad 0 \le m,\ n < N \tag{9}$$

For a clutter pixel $c(m, n)$, it includes reflections from minute scatters inside this resolution cell. For modern coherent imaging radar with a quadrature receiver, it can be represented as:

$$
\begin{aligned}
c(m, n) &= \sum_{k=1}^{K} a_k \exp(j 2\pi f_c \tau_k) \\
&= c_r + j c_i
\end{aligned}
\tag{10}
$$

where a_k and τ_k are the magnitude and relative two-way propagation delay of the reflection from the k-th scatter in this clutter resolution cell. If we assume those variables are statistically independent and K is large, according to Central limit theorem the sum in (10) tends to be a complex Gaussian random variable, and its amplitude is approximately Rayleigh distributed [13, 16, 17]. Although, for high-resolution radar with a low gazing angle, the amplitude is closer to be Weibull distributed for ground clutters, Rayleigh approximation is accurate enough, especially for the distribution near the mean [15].

Another important assumption about SAR clutters is that clutters in different pixels are statistically independent [13–16]. Therefore, we have:

$$E\left[c(m, n) c^*(p, q)\right] = \sigma_c^2 \delta(p - m)\delta(q - n) \tag{11}$$

where σ_c is the clutter standard deviation, and δ is the Dirac function.

Using ergodic characteristics of independent identical random variables, the statistical mean value in (11) can be approximated with a spatial average:

$$E\left[c(m,n)c^*(p,q)\right] \cong \sum_k \sum_l c(k,l)c^*(k+p-m,l+q-n)$$

$$\cong \sigma_c^2 \delta(p-m)\delta(q-n) \tag{12}$$

·From (12) we find the clutters are spatially uncorrelated, which provide clutters a distinct feature from the target signal. But we must note that for SAR clutters there is some weak correlation among adjacent pixels, thus (12) is not quite right if $p-m$ and $q-n$ are close to zeros.

Generally the target area is in the central part of a SAR image, and the clutters are located in surrounding parts. We define that the target signal is zero in clutter area, and the clutter is zero in target area, i.e.,

$$t(m,n) = 0, \quad (m,n) \text{ in clutter area} \tag{13}$$

$$c(m,n) = 0, \quad (m,n) \text{ in target area} \tag{14}$$

Because zero values don't contribute anything to the summation in (12), the definition in (14) doesn't affect the autocorrelation property of clutters in (12) as long as there are enough actual clutter samples in the correlation. Also the zeros in (13) won't affect the autocorrelation property of target image.

Considering (9), (13), and (14), we have:

$$s(m,n) = t(m,n) + c(m,n) \quad 0 \le m,\ n < N \tag{15}$$

With the additive model in (15) for a SAR image, we need to find the best wavelet packet basis to maximize Signal-to-Clutter ratio in the transform domain.

3.2 Best Wavelet Packet Basis for Maximization of Signal-to-Clutter Ratio

If we apply a wavelet packet basis shown in (6) to a SAR image $s(m,n)$ in (15), the transform coefficients are:

$$\widetilde{S}_{p,q}^j(k,l) = \sum_m \sum_n s(m,n)U_{p,q}^j(k-2^jm,l-2^jn)$$

$$= \widetilde{T}_{p,q}^j(k,l) + \widetilde{C}_{p,q}^j(k,l) \tag{16}$$

where:

$$\widetilde{T}_{p,q}^{j}(k,l) = \sum_m \sum_n t(m,n) U_{p,q}^j(k - 2^j m, l - 2^j n) \qquad (17)$$

$$\widetilde{C}_{p,q}^{j}(k,l) = \sum_m \sum_n c(m,n) U_{p,q}^j(k - 2^j m, l - 2^j n) \qquad (18)$$

are the coefficients for target image and clutters, respectively.

Because a liner combination of independent Gaussian random variable, the clutter coefficients still are Gaussian distributed. If we rewrite (18) into a simple form, and note that wavelet packet basis is orthonormal, there are:

$$\widetilde{C}(k,l) = \sum_m \sum_n c(m,n) U(k,l,m,n) \qquad (19)$$

and

$$
\begin{aligned}
E&\left[\widetilde{C}(k,l)\widetilde{C}^*(i,j) \right] \\
=& E\left[\sum_m \sum_n c(m,n) U(k,l,m,n) \sum_p \sum_q c^*(p,q) U(i,j,p,q) \right] \\
=& \sum_m \sum_n \sum_p \sum_q E\left[c(m,n)c^*(p,q) \right] U(k,l,m,n) U(i,j,p,q) \\
=& \sum_m \sum_n \sum_p \sum_q \sigma_c \delta(p-m)\delta(q-n) U(k,l,m,n) U(i,j,p,q) \\
=& \sum_m \sum_n \sigma_c U(k,l,m,n) U(i,j,m,n) \\
=& \sigma_c \delta(i-k)\delta(j-l) \qquad (20)
\end{aligned}
$$

Therefore, the clutter coefficients are uncorrelated, thus independent Gaussian statistical variables with the same mean and variance as those of the clutter in spatial domain.

We have demonstrated that the statistical characteristics of SAR image clutters don't change after wavelet packet basis transformation. But target image is correlated to itself. We need to find a wavelet packet basis to make transformed target image further concentrated, and increase the signal-to-clutter ratio in transform domain, in other words, we need to make transformed target image sparse. A cost functions is needed to measure the sparsity of the transformed signal, thus

the best wavelet packet basis can be found for a specific image to achieve the maximum sparsity in the transformed image. A typical cost function for sparsity is entropy function. But entropy function itself is not an additive cost function, which makes it inapplicable in a fast global best basis search algorithm. A modified additive entropy function was proposed [18, 19], but it requires computation-intensive logarithm operation to evaluate function cost, and is unstable in the environment with clutter or noise interference. Alternatively we use l^p energy concentration function as cost function in this application. The l^p energy concentration function of a data sequence $\{x(k),\ k=1,2,\ldots,K\}$ is defined as:

$$C = \sum_{k=1}^{K} |x(k)|^p \qquad 0 < p < 2 \tag{21}$$

For a transformed SAR image with a coefficient matrix $\left[\widetilde{S}\right]$, the cost function is:

$$C = \sum_{k}\sum_{l} \left|\widetilde{S}(k,l)\right|^p \qquad 0 < p < 2 \tag{22}$$

For convenience and efficiency, we usually choose: $p = 1$ in (22). Supposing we transform a sequence $\{x_1, x_2, \cdots, x_L\}$ into another sequence $\{\tilde{x}_1, \tilde{x}_2, \cdots, \tilde{x}_L\}$ with a wavelet packet basis using the cost function of (22), the transformed sequence is the sparsest if all of them excerpt one are zeros, accordingly the cost is the minimum in this case. We illustrate the best basis selection criterion based on the energy concentration cost function in (21) using a simple case: assuming that a data sequence is $\{x_1, x_2\}$ with energy equal to 1, and its orthonormal basis transform coefficients are $\{\tilde{x}_1, \tilde{x}_2\}$, we have:

$$|\tilde{x}_1|^2 + |\tilde{x}_2|^2 = 1 \tag{23}$$

The cost function is:

$$Cost = |\tilde{x}_1| + |\tilde{x}_2| \tag{24}$$

As shown in Figure 1, transformed data must be a point on the circle with radius of 1 because of constant energy constraint. The Lines a, b, and c are the energy concentration cost functions with $p = 1$. The cost function lines must cross the one-fourth of the circle to satisfy
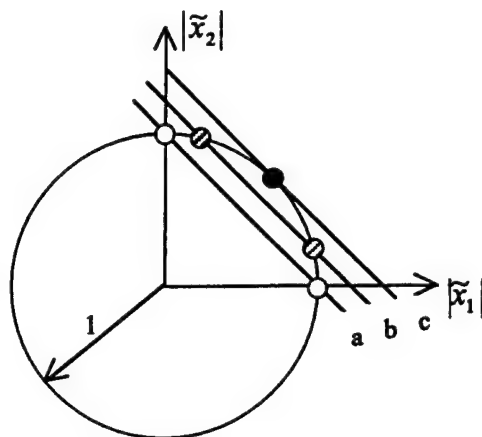
Figure 1. Relationship between the sparsity of a basis transformed signal and the energy concentration cost function.

the energy constraint. Apparently on Line c the blank point is the transformed data, but it has the highest cost, and worst sparsity. On Line a, two white points are the possible transformed data. They have the lowest cost, and best sparsity for all possible basis transformation. The gray points on Line b are the transformed data with cost and sparisty between the best and the worst. Therefore, based on the energy concentration cost function, we can effectively find the best transform basis to maximize the sparsity of the transformed signals.

Due to the non-overlapping of target and clutter in spatial domain, mostly the coefficients for target and clutter are also separated in the finer scales in the transform domain. Thus the total cost of the transformed SAR images in (16) is approximately equal to the sum of the costs of transformed target images and clutters, i.e.,

$$Cost\left(\left[\widetilde{S}\right]\right) \cong Cost\left(\left[\widetilde{T}\right]\right) + Cost\left(\left[\widetilde{C}\right]\right) \tag{25}$$

where $\left[\widetilde{S}\right]$, $\left[\widetilde{T}\right]$, and $\left[\widetilde{C}\right]$ are the transform coefficient matrices for the whole SAR image, target image, and clutters, respectively. The cost of transformed clutters doesn't change because they are the random variables with exactly the same distribution as that of the original clutters in spatial domain. The minimization of the cost of the whole transformed SAR image is equivalent to the minimization of that of the transformed target image, and thus the maximization of target signal-to-clutter ratio in the transform domain.

3.3 Implementation of Adaptive Wavelet Packet Transform for SAR Images

Theoretically we can apply every possible wavelet packet basis to a SAR image, evaluate the cost of the every transformed image, and find the best wavelet packet basis with the least cost. But the brutal force computation is impractical to implement because there are too many eligible wavelet packet bases for a specific application and the direct convolution in (7) is computationally too costly. Fortunately, in [18] a fast decomposition algorithm was proposed to search the best wavelet packet for a data sequence based on additive cost function, and it can be readily adapted to 2-D SAR image processing.

Generally the original SAR image is the discretized samples using pulse basis, and it can be approximated as the coefficients of wavelet packet basis with the highest spatial resolution, i.e., in the finest scale. The decomposition coefficients in the next scale are related to the ones in current scale by "2-scale equations" using a pair of quadrature filters $\{h(n)\}$ and $\{g(n)\}$.

Assuming that the initial image samples are represented with a matrix [S], its decomposition coefficients at the next scale can be obtained through the convolution and down-sampling of [S] and quadrature filter impulse responses $\{h(n)\}$ and $\{g(n)\}$, i.e.,

$$S_{HH}^{(2)}(m,n) = \sum_k \sum_l s(k,l)g(2m-k)g(2n-l)$$

$$S_{LH}^{(2)}(m,n) = \sum_k \sum_l s(k,l)h(2m-k)g(2n-l)$$

$$S_{HL}^{(2)}(m,n) = \sum_k \sum_l s(k,l)g(2m-k)h(2n-l)$$ \quad (26)

$$S_{LL}^{(2)}(m,n) = \sum_k \sum_l s(k,l)h(2m-k)h(2n-l)$$

where $\{h(n)\}$ and $\{g(n)\}$ denote the impulse responses of low- and high-pass Quadrature Filters (QFs), respectively. The decomposition in (26) is widely referred as quadtree decomposition, which is illustrated in Figure 2. The quadtree decompositions can be applied recursively until the coarsest scale is reached. Apparently the decomposition at each scale needs $O(N^2)$ operations, and the number of total available scales is about $\log_2(N)$. Therefore, the total computation cost to implement the full decomposition from spatial domain to frequency
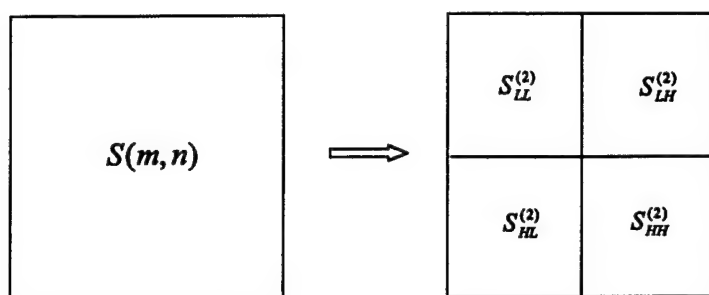
Figure 2. Quadtree decomposition structure.

domain is about $O(N^2\log_2 N)$ operations using the quadtree decomposition method. Because the cost function is additive, the best wavelet packet basis and corresponding transform coefficients can efficiently found from the fully quadtree decomposed result. With regard to a SAR image the procedures to find the best wavelet packet basis and the transform coefficient are as follows:

1. Fully decompose the initial image into frequency domain using quadtree decomposition.
2. Use the wavelet basis at the last scale as the best initial basis, and its cost as the best initial cost.
3. Trace back from the last scale, and comparing the cost at every node with the smallest cost in the all branches decomposed from the node. If the cost is reduced, update the best basis and the corresponding cost using this node; otherwise continue the backward search for the best basis.
4. The best basis and its transformed coefficients are found when the search comes toward the first scale, i.e., the initial spatial sampling data.

4. PROCESSING RESULTS

With the principles described, the clutter in a specific SAR image can be removed in the wavelet packet basis domain. The clutter removal is implemented by thresholding processing in the transform domain with a higher Signal-to-Clutter ratio compared with direct thresholding in spatial domain. But even the thresholding processing in transform domain will inevitably cause the target image loss, while the clutter is suppressed. In the processing, we choose a threshold level to keep

target image loss under an acceptable level, and allow some clutter residues to exist after the processing. The clutter residues can be easily removed by some post-processing such as additional thresholding and clustering processing in spatial domain. The processing scheme for SAR clutter reduction using AWPT method is shown in Figure 3. This clutter reduction scheme is applied to standard MSTAR SAR images [12]. A typical focused MSTAR image with clutters is shown in Figure 4. The image size is 128×128, and the resolution is about $0.3\,\mathrm{m} \times 0.3\,\mathrm{m}$. The target in the image is BTR-70 transportation vehicle, and the clutter was generated from background vegetation scattering. From the image, we can find that the reflections from the rear part of this vehicle are weak and indistinguishable from the background clutters due to the signal blockage by the front part of the target. It would be difficult to remove all clutters and keep the whole target signal intact using direct thresholding method.

4.1 Wavelet Filter for SAR Image Transform

Wavelet packet transform of an image can be implemented by recursive quad-tree decomposition of the original spatial sampling data. Based on "two-scale equations," the coefficients in the coarser scales can be derived from the coefficients in the finer scales. Considering the original sampling SAR data as the transform coefficients with the finest scale in spatial domain, we can obtain all wavelet packet transform coefficients by repeatedly filtering and down-sampling of the original spatial image using a wavelet filter. To maximally concentrate the energy of the transformed image, we choose Daubechies wavelet filter in this application. It is the most commonly used orthonormal wavelet filer; and the corresponding wavelet basis functions possess localization property in both time and frequency domains. The order of the wavelet filter is related to the vanishing moments of the wavelet basis functions. The higher the wavelet filter order, the more vanishing moments the basis functions, thus the more concentrated the transformed coefficients. However, through the convolution operation, the finest spatial resolution available for the transformed coefficients is the order of the wavelet filter. For a SAR image with scattering points in high spatial resolution, the wavelet filter of low order is desired for efficient representation of those scattering points in the transform domain. Therefore, we choose Daubechies filter with the order of 6 as the wavelet filters in this application. Using the AWPT algorithm based on
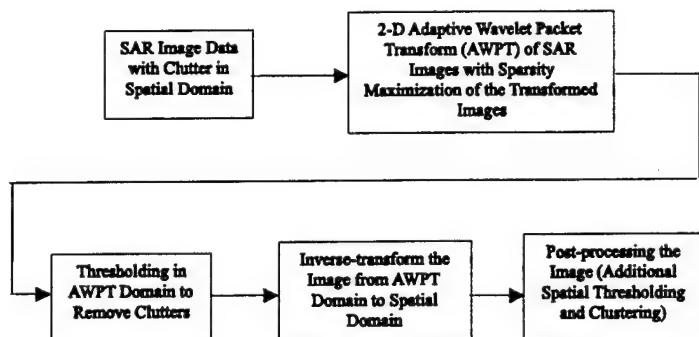
Figure 3. The processing scheme of automatic SAR clutter reduction based on Adaptive Wavelet Packet Transform (AWPT).

Figure 4. SAR image for BTR-70 transportation vehicle with vegetation clutters.

the quad-tree decomposition, we transformed BTR-70 image in Figure 4 into AWPT domain. The transformed image is displayed in Figure 5. The value of the corresponding energy concentration cost function is about 595 for the best wavelet packet basis, opposed to 777 of the cost function value in spatial domain; while the cost function value is about 641 if the conventional wavelet transform is applied to the image. Apparently we achieve the sparsest transformed image using the AWPT algorithm.

Figure 5. The basis transformed BTR-70 SAR image using AWPT.

4.2 Frequency-Dependent Thresholding

To remove clutters in the AWPT domain, we need to apply a threshold level to the transformed coefficients of SAR images. The common thresholding method is the soft-shrinkage proposed in [10], in which the above-threshold signal amplitude is reduced by a level of the threshold. The soft-thresholding is generally applicable to the cases that signals and noise or clutter are spatially overlapping. For SAR images, the target image and clutters are basically non-overlapping even in the transform domain. Hard-thresholding is a better choice, and it is defined as follows:

$$
\hat{\widetilde{S}}(m,n) = \begin{cases} \widetilde{S}(m,n) & \text{if } \left| \widetilde{S}(m,n) \right| > T \\ 0 & \text{if } \left| \widetilde{S}(m,n) \right| \le T \end{cases} \tag{27}
$$

where: T is the threshold level.

If the spatial clutters are white and Gaussian distributed, the transformed clutters, as we have demonstrated, are still white and Gaussian distributed. Based on Newman-Pearson Criterion [15], the best threshold level is a constant provided that it meets requirements for

probabilities of false-alarm and target detection. But for SAR images, a pixel has some weak correlation with its adjacent pixels. Therefore, the clutter on a SAR image is not really white, and its power spectrum is stronger in lower frequencies. We design the threshold levels that are dependent on the central frequency for the quad-tree decomposition outputs at each of the final branches. For the output of one of out-ermost branches of the quad-tree decomposition, the central vertical and horizontal frequencies are assumed to be f_V and f_H, respectively, and the central frequency at that output branch is considered to be:

$$f_C = \sqrt{f_V^2 + f_H^2} \tag{28}$$

From quad-tree decomposition structure, we can find out the frequencies f_V and f_H, noting that due to the down-sampling, for two-channel decomposition of higher frequency band data, the high frequency components come out from low frequency filter output; while the low frequency components from high frequency filter outputs. Therefore the threshold level for the quad-tree decomposition output branch with central frequency f_C is:

$$T(f_C) = \frac{C \cdot \sigma_C}{\beta + f_C^\alpha} \tag{29}$$

where C is a constant, σ_c is the clutter standard deviation, and α and β are the parameters used to fit the mode to actual clutters. Therefore, the threshold level is the largest in low frequency, and the smallest in high frequency. Due to hard-thresholding processing, there is no DC energy loss for target image even with a high threshold level in near-DC areas. For MSTAR image processing we choose: $\alpha = 0.8 \sim 1$, and $\beta = 0$ in (29) to approximate the clutter spectrum characteristics and achieve the best clutter rejection performance. The AWPT transformed BTR-70 image is thresheld with parameters: $C = 0.5$, $\alpha = 0.85$, and $\beta = 0$ in (29), and shown in Figure 6. Using frequency-dependent threshold, we still can keep the delicate high-frequency components, which represent the important point-scattering reflections in the SAR images. But we could lose or blur the point-scattering signals after the processing if just using a constant threshold level for all transformed coefficients.
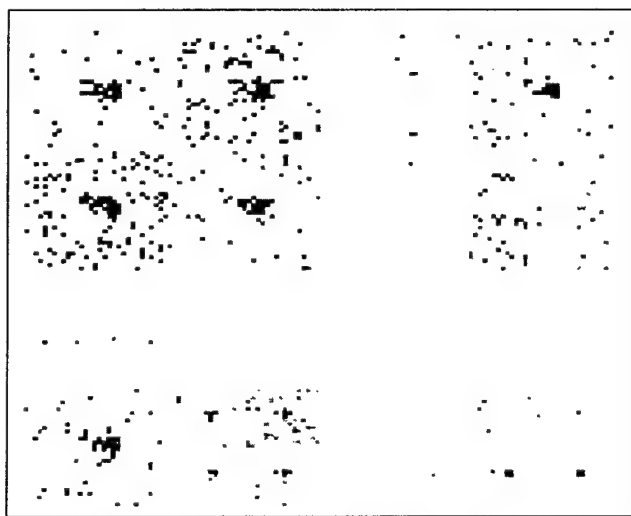
Figure 6. The transformed BTR-70 SAR image after frequency-dependent thresholding processing.

4.3 Post-Processing

Through thresholding processing most SAR image clutters are eliminated in the AWPT domain. The original SAR images can be restored by inverse-transforming the wavelet coefficients to spatial domain based on the same basis in the quad-tree decomposition. Similarly the inverse-transform can be efficiently implemented with filtering and up-sampling using another pair of filters $\{P(n)\}$ and $\{Q(n)\}$. Even with thresholding processing in AWPT, there are still some clutter residues existing. After the inverse-transform, those clutter resides will spread over SAR domain. Therefore, a second small threshold and a clustering processing are applied to the restored SAR image to further improve clutter rejection performance. The clustering algorithm replaces with zeros any connected non-zero blocks that have fewer elements than a pre-defined block size. Usually we set the block size to larger than the clutter residue sizes and smaller than target block size. For MSTAR images a clustering block size of 32 is usually enough to eliminate all clutter residues. Figure 7 is the restored BTR-70 image through post-processing with a second threshold level of about $0.1\sigma_c$. Also the best processing result using direct thresholding and clustering processing is shown in Figure 8. Apparently an essential part of the
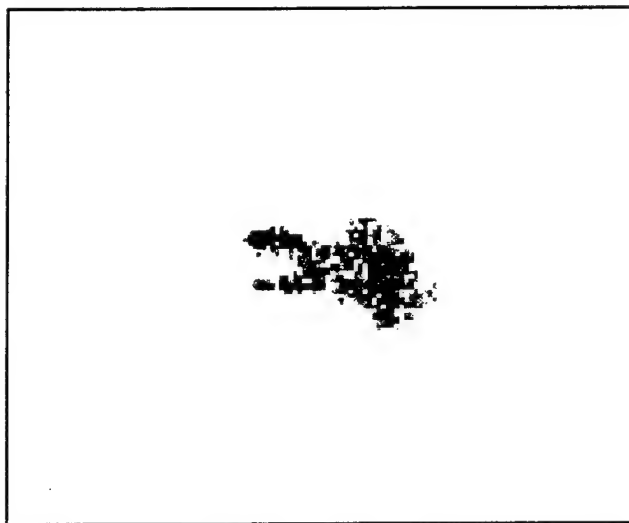
Figure 7. The restored BTR-70 image with thresholding in AWPT domain and post-processing in spatial domain.
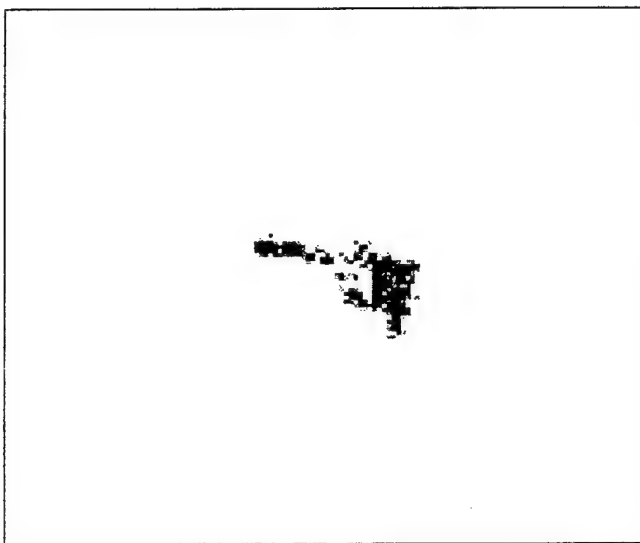
Figure 8. The de-cluttered BTR-70 image with direct thresholding processing in spatial domain.

target is lost in the direct thresholding processing because of low signal-to-clutter ratio in spatial domain, which thus poses a threat to correct target identification afterwards. Through the AWPT processing, the whole original target image is kept, while the clutters are completely removed.

4.4 Performance Metrics for MSTAR Data Processing

For a SAR image recovery processing the clutter rejection performance of an algorithm can be measured based on the ratio of mean square error to clutter standard deviation. But in the cases of absence of the original reference signals as for MSTAR images, the improvement of average target image signal-to-clutter ratio is a reasonable substitute. We define average target Signal-to-Clutter Ratio (SCR) as:

$$SCR = \frac{\sum_i \sum_j \left| \hat{S}(i,j) \right|}{N\sigma_C} \tag{30}$$

where $\hat{S}(i,j)$ is the processed target pixel, N is the total number of target image pixels, and σ_c is the clutter standard deviation.

The clutter rejection performance of an algorithm can be measured based on SCR improvements through its processing. In the AWPT clutter rejection processing, we gradually increase the AWPT domain threshold level, and measure the SCR improvements due to the thresholding processing in the AWPT domain (prior to the post-processing), while keeping the target image loss inside an acceptable range. Figure 9 shows SCR vs. the target image loss for three different kinds of MTSAR images through the AWPT processing. Target Image Loss (TIL) is defined as:

$$TIL = \frac{\overline{S} - \overline{\hat{S}}}{\overline{S}} \tag{31}$$

where $\overline{S}$ and $\overline{\hat{S}}$ are the average target signal amplitudes before and after the processing, respectively. For comparisons the SCR vs. TIL curves for Conventional Wavelet Transform (CWT) and direct thresholding are plotted in the same figures. We find that for a fixed target image loss, the AWPT algorithm almost always performs better than the CWT or direct thresholding method.
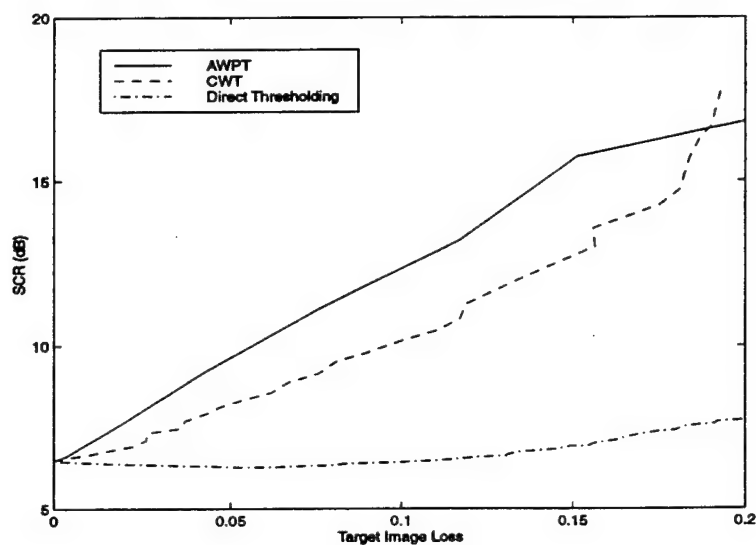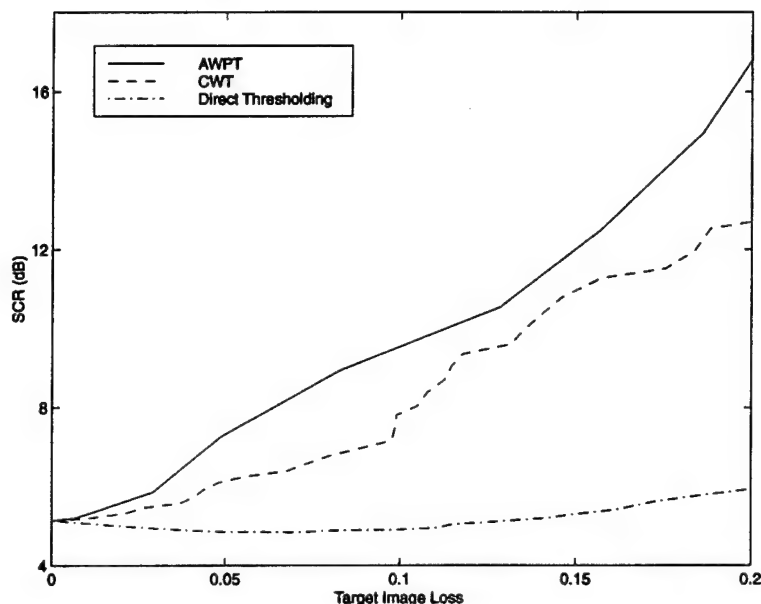
(a)
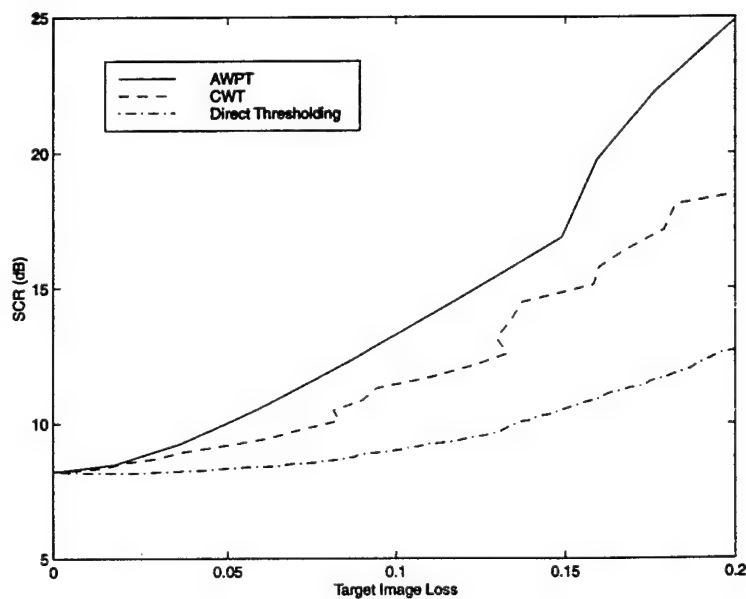
(b)

Figure 9. Signal-to-Clutter Ratio vs. target image loss using AWPT, CWT and direct thresholding methods for (a) BTR-70, (b) T-72, and (c) BMP-2 targets.

(c)

Figure 9. Continued.

5. CONCLUSIONS

We have developed a new clutter-rejection algorithm for SAR images based on Adaptive Wavelet Packet Transform (AWPT). It transforms the basis function of the SAR images from the regular pulse basis to a wavelet packet basis to make the transformed coefficients maximally concentrated on the transform domain. The transformed image has a higher target Signal-to-Clutter Ratio (SCR) compared with that in conventional spatial domain, thus the clutters can be removed in transform domain with less target signal losses. The method is based on the basic assumption that a clutter pixel in a SAR image is not or weakly correlated with one another; while target signals are strongly correlated to themselves. Thus, the SCR improvements are made possible through basis transformation.

The energy concentration function is used as the cost function to find the best wavelet packet basis to make the transformed coefficients with the maximum SCR. The best basis search and the basis transfor-

mation for an image can be efficiently implemented using 2-D quad-tree decomposition algorithm. To search the best wavelet packet basis for a SAR image with clutters, it is very important to ensure either that the clutters and the target image are approximately non-overlapping after transformation in transform domain; or that the target energy is significantly stronger than the clutter one. Hence the best wavelet packet decomposition trees can be dominated by the target signals; otherwise the AWPT algorithm is not applicable.

A frequency-dependent thresholding method is introduced because the clutters in a SAR image are weakly correlated, i.e., they are "colored" rather than "white," as commonly assumed. The threshold level for the AWPT transformed outputs are chosen based on the central frequency of the data in this output. The lower the central frequency, the higher the threshold level. Simulation results show that the careless thresholding could degrade the performance of the AWPT algorithm to that of conventional wavelet transform, or even worse.

Processing results on MSTAR images show that this algorithm is very effective to remove the clutters for a SAR image with only limited clutter information such as standard deviation and rough spectrum characteristics required. With robust parameters pre-selected, the AWPT algorithm can be used to automatically remove the clutters in a large number of SAR images. But for the conventional direct thresholding method, it is usually very difficult to find a threshold level to remove all background clutters and keep the whole target image unaltered. This new method is also very useful for the situations in which the classical direct thresholding method might not work at all. Those situations include that some parts of target image signals are weaker than the clutter, or that the target signals and clutters are spatially over-lapping resulting from un-focused processing, or multi-path effects.

ACKNOWLEDGMENT

REFERENCES

1. Wehner, D. R., *High Resolution Radar*, Artech, Norwood, MA, 1995.

2. Pham, D. H., A. Ezekel, M. T. Campbell, and M. J. T. Smith, "A new end-to-end SAR ATR system," *Proceedings of SPIE: Algorithms SAR Imagery VI*, Vol. 3721, 292–301, Orlando, Florida, April 1999.

3. Luo, D., *Pattern Recognition and Image Processing*, Horwood Publishing Limited, Chichester, England, 1998.

4. Wickerhauser, M. V., *Adapted Wavelet Analysis from Theory to Software*, A. K. Peters, Wellesley, Mass., 1994.

5. Chui, C. K., *An Introduction to Wavelets*, Academic Press, New York, 1992.

6. Daubechies, I., *Ten Lectures on Wavelets*, SIAM, Philadelphia, Penn., 1992.

7. Coifman, R. R., Y. Meyer, and M. V. Wickerhauser, "Wavelet analysis and signal processing," In *Wavelets and Their Applications*, 153–178, Jones and Barlett, Boston, 1992.

8. Mallat, S., *A Wavelet Tour of Signal Processing*, Academic Press, Inc., New York, 1998.

9. Deng, H. and H. Ling, "Fast solution of electromagnetic integral equations using adaptive wavelet packet transform," *IEEE Trans. Antennas Propagat.*, Vol. 47, 674–682, April 1999.

10. Donoho, D. L. and I. M. Johnstone, "Ideal spatial adaption by wavelet shrinkage," *Biometria*, Vol. 81, 425–455, Dec. 1994.

11. Odegard, J. E., H. Guo, M. Lang, C. S. Burrus, R. O. Wells, Jr., L. M. Novak, and M. Hiett, "Wavelet based SAR speckle reduction and image compression," Research Report, Comp. Math Lab., Rice Univ., and MIT Lincoln Lab., 1995.

12. *MSTAR SAR Data Set, Clutter and Targets*, collected by Sandia National Lab, released by DARPA, Apr. 1997.

13. Moulin, P., "A wavelet regularization method for diffuse radar-target imaging and speckle-noise reduction," *J. Math. Imag. and Vision*, No. 3, 123–134, 1993.

14. Irving, W. W., L. M. Novak, and A. S. Willsky, "A multiresolution approach to discrimination in SAR imagery," *IEEE Trans. Aerospace and Elec. Systems*, Vol. 33, No. 4, 1157–1168, Oct. 1997.

15. Skolnik, M. I., (Ed.), *Radar Handbook*, 2nd edition, McGraw-Hill, New York, 1990.

16. Van Trees, H. L., *Detection, Estimation, and Modulation Theory*, Part III, John Wiley & Sons, New York, 1971.

17. Papoulis, A., *Probability, Random Variables, and Stochastic Processes*, McGraw-Hill, New York, 1965.

18. Coifman, R. R. and M. V. Wickerhauser, "Entropy-based algorithms for best basis selection," *IEEE Trans. Info. Theory*, Vol.

38, 713–718, March 1992.

19. Donoho, D. L., "On minimum entropy segmentation," in *Wavelets: Theory, Algorithms, and Applications,* Academic Press, Inc., New York, 1994.

Clutter Reduction for Synthetic Aperture Radar Images Using Adaptive Wavelet Packet Transform

Hai Deng[*] and Hao Ling
Department of Electrical and Computer Engineering
The University of Texas at Austin
Austin, TX 78712-1084

1.Introduction

Synthetic Aperture Radar (SAR) images of ground targets generally consist of target features and clutters from background scattering [1]. In automatic target recognition (ATR) applications, it is desirable to remove the clutter from the target image before ATR processing. The standard way to suppress clutter is to apply an appropriate threshold level to the whole SAR image. However, this approach assumes that the target signal-to-clutter ratio (SCR) is large enough. Otherwise this direct threshold approach results in either target feature loss or remnant clutter residue. In this work, we set out to develop a decluttering algorithm to automatically extract the target image from a SAR image by maximizing the SCR using the adaptive wavelet packet transform (AWPT) [2]. The wavelet packet basis is a generalization of the conventional wavelet basis [3] and has been applied for image compression [4] and moment matrix sparsification [5].

Our approach is to transform the SAR image to a new domain using the wavelet packet basis. Since a typical target image usually consists of point scatterers and more diffused region features, the multi-scaled wavelet basis is well suited to focus the target image. Clutter image, on the other hand, is statistically uncorrelated from pixel to pixel, and the transformed clutter image under the same set of bases remains unfocused. Therefore, we expect that the SCR can be increased by transforming the original image by an appropriately chosen set of wavelet packet basis. The cost function of our AWPT algorithm is chosen to describe how well the target signal is focused in the transform domain. An efficient basis search algorithm is implemented to find the best wavelet packet basis. Our algorithm is tested using the MSTAR SAR data set [6] and results show that an improved SCR can be achieved using the AWPT algorithm.

2. SAR Image Representation with Wavelet Packet Basis

A discrete 2-D SAR image s(m, n) can be represented as:

$$s(m,n) = t(m,n) + c(m,n) \quad 0 \leq n, m < N \qquad (1)$$

where t(m, n) and c(m, n) denote the target image and the clutter in the SAR image, respectively. We define a set of orthogonal and complete 2-D wavelet packet basis functions:

$$\{U^j_{p,q}(k,l) \quad 0 \leq j < J, \ 0 \leq p,q < 2^j, \ 0 \leq k,l < N2^{-j}\} \qquad (2)$$

where j denotes the scale index, $J=\log_2(N)$, p, q are the modulation indices, and k, l are the position indices. The 2-D wavelet packet basis function can be generated from the product between two 1-D wavelet packet bases:

$$U_{p,q}^j(k,l) = \psi_p^j(k)\psi_q^j(l) \tag{3}$$

ψ is a 1-D wavelet packet basis that can be generated from the scaling function and the basic wavelet function using the "2-scale equation" [3-5].

The transformation of a SAR image $s(m, n)$ using the wavelet packet basis is thus:

$$\begin{aligned}
\tilde{S}_{p,q}^j(k,l) &= \sum_m \sum_n s(m,n)U_{p,q}^j(k-2^jm,l-2^jn) \\
&= \sum_m \sum_n t(m,n)U_{p,q}^j(k-2^jm,l-2^jn) + \sum_m \sum_n c(m,n)U_{p,q}^j(k-2^jm,l-2^jn) \\
&= \tilde{T}_{p,q}^j(k,l) + \tilde{C}_{p,q}^j(k,l)
\end{aligned} \tag{4}$$

where $\tilde{T}$ and $\tilde{C}$ are the transform coefficients of the target image and the clutter in the image with the wavelet packet basis.

If we define the SCR of a SAR image as the ratio of the average target amplitude to the standard deviation of the clutter, the SCR of the image before and after the transform are $\bar{t}/\sigma(c)$ and $\bar{\tilde{T}}/\sigma(\tilde{C})$, respectively. The clutter function $c(m, n)$ represents the reflectivity of different pixels in the background, and is assumed to be independent and identically distributed [7]. It can be shown that its wavelet packet transform coefficients $\tilde{C}$ are still uncorrelated [8], and that the standard deviation of the clutter does not change after the basis transform. On the contrary, signals from the target area are strongly correlated and it is possible to increase target energy concentration with a basis transformation. Therefore, with a given SAR image we need to search and find the best wavelet packet basis to maximize the amplitude of the transformed target image.

3. Adaptive Search Procedure and Implementation

To find the best wavelet packet basis and implement the basis transform, we need to define a cost function to describe how well the transformed target signal is concentrated with a wavelet packet basis. The best basis is the one that generates a transformed signal having the least cost. The most commonly used cost function is the entropy function. Because of the complexity of evaluating the entropy function, we use the energy concentration function as our cost function in this application. For a transformed SAR image it is defined as:

$$Cost = \sum_{j,p,q} \sum_{k,l} \left| \tilde{S}_{p,q}^j(k,l) \right| \tag{5}$$

Because there are many possible wavelet packet bases in (2) for the transform, it is impractical to try each of them to find the best basis. An effective quad-tree decomposition algorithm was generalized from that proposed in [9] to find the best 2-D wavelet packet basis. The algorithm decomposes the original image using 2-channel filtering with a pair of quadrature filters through all scales from the space domain to the spectral domain. With the cost labeled at every branch, the decomposition tree is then "pruned" back along each branch from the last scale toward the earlier scales. The pruning process is accepted whenever it leads to a lower cost. The best decomposition tree can be found after the search

1781

process with a total computational complexity of about $O(N^2 \log N)$. A scale-dependent threshold is then applied to the transformed image. Because there is a weak correlation between clutter samples, we increase the threshold level slightly as the scale increases. The threshold level is chosen as:

$$Th_j = K\sigma\sqrt{j/J} \qquad (6)$$

where j is the scale index, σ is the clutter standard deviation, and K is a constant. With thresholding, most of the clutter is removed in the wavelet packet basis domain, and the image is inverse-transformed back to the SAR domain to restore the original target image using the same tree from the decomposition. Although the SCR is much improved in the restored image, it is not possible to remove the clutter completely through such processing. We apply a very small second threshold to the restored image, and then use a standard clustering algorithm to get rid of clutter residues.

4. Test Results

To test the effectiveness of the AWPT processing, we apply it to the MSTAR SAR image data set. Fig. 1 shows an MSTAR image in which the target is a ground vehicle and the clutter is due to vegetation. There are several strong point scatters in the front of the vehicle, but the scattering from the back part is relatively weak. Fig.2 shows the result of applying the direct thresholding method to the image. Fig. 3 shows the decluttered image by applying the AWPT algorithm. We choose Daubechies filter with order of 6 as the wavelet filter, and the processing parameters used are K=1 and 0.05σ for the second threshold. By visually comparing Figs. 2 and 3, we note that some crucial features of the target are kept in the AWPT-processed image. In both processing methods, there is some target information loss. Fig. 4 shows the signal-to-clutter ratio versus average target image loss for the two processing methods. It is observed that for a fixed target image loss the AWPT method always achieves a higher SCR value than the direct thresholding method. Similar results are obtained when the algorithm is applied to other MSTAR data.

References
[1] D. R. Wehner, *High Resolution Radar*, Artech, Norwood, MA, 1995.
[2] M. V. Wickerhauser, *Adapted Wavelet Analysis from Theory to Software*, A.K.Peters, Wellesley, Mass. 1994.
[3] C. K. Chui, *An Introduction to Wavelets*. Academic Press, New York, 1992.
[4] R. R. Coifman, Y. Meyer, and M. V. Wickerhauser, "wavelet analysis and signal processing." In *Wavelets and their applications*, pp. 153-178, Jones and Barlett, Boston, 1992.
[5] H. Deng and H. Ling, "Fast solution of electromagnetic integral equations using adaptive wavelet packet transform," to appear in *IEEE Trans. Antennas Propagat., 1999*.
[6] MSTAR SAR data set, clutter and targets, collected by Sandia National Lab, released by DARPA, Apr. 1997.

[7] H. L. Van Trees, *Detection, Estimation, and Modulation Theory, Part III,* Wiley, New York, 1971.

[8] P. Moulin, "A wavelet regularization method for diffuse radar-target imaging and speckle-noise reduction," *J. Math. Imag. and Vision,* pp. 123-134, No. 3, 1993.

[9] R. R. Coifman, and M. V. Wickerhauser, "Entropy-based algorithms for best basis selection," *IEEE Trans. Info. Theory,* Vol. 38, pp.713-718, March 1992
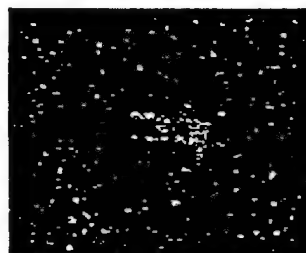
Fig. 1. SAR image of a ground vehicle with clutter

Fig. 2. Clutter rejection using the direct thresholding method
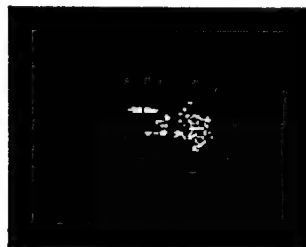
Fig.3. Clutter rejection using the AWPT approach.
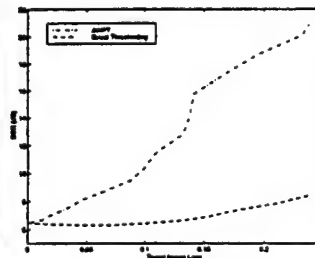
Fig. 4. SCR vs. target image loss for the two processing methods.

Dynamic Signature Simulation Using the Shooting and Bouncing Ray Technique

Rajan Bhalla*, Hao Ling and Jim Schmitz⁺

Department of Electrical and Computer Engineering
The University of Texas at Austin
Austin, TX 78712 U.S.A

⁺DEMACO Inc.
Dayton, OH U.S.A.

Abstract

Methodologies for simulating the radar signatures of moving ground targets using the shooting and bouncing ray (SBR) technique are investigated. The motions of interest include both target movement as a whole with respect to background and sub-component motion such as those due to wheels and turrets. The brute-force method to predict the multi-pulse radar signature is to simulate the target range profiles at N different dwell time instances. To carry out the brute-force computation, we first generate N CAD models of the target representing the states of the target and compute the range profiles for all N models. Not only is the first step a tedious process, the second step requires a computation time that is N times longer than that for a single range profile. Furthermore, a completely new run must be carried out for a new set of motion parameters. Therefore, two alternate approaches are investigated to more rapidly carry out dynamic signature simulation.

The first approach is based on an extrapolation algorithm. It is an extension of the signature extrapolation algorithm for target look that we have developed previously for SBR (Bhalla and Ling, J. Electromag. Waves Applications, Feb. 1996). In this approach we launch rays only once at the target. Given the ray history and the target motion, we use the differential Doppler information for each ray to predict its contribution at N time instances. The extrapolation algorithm requires only a single ray trace. However, a completely new run must still be carried out for a new set of motion parameters.

The second approach is to use the extracted 3D scattering center set (Bhalla and Ling, IEEE Trans. Antennas Propagat., Nov. 1996) from the target to predict the dynamic signature. During the extraction process, each scattering center is tied back to the component surfaces on the target that gave rise to that scattering center. It is then possible to infer the motions onto the individual scattering centers associated with the component. Using this approach, we can rapidly predict the target range profiles at the N time instances. In addition, it is easy to carry out this procedure for arbitrary target/component motions at little additional computation cost. Dynamic simulation results for ground targets with various motion parameters using the different approaches will be presented.

Comparison of high-resolution ISAR imagery from measured data and synthetic signatures

Junfei Li[*a], Yuanxun Wang[a], Rajan Bhalla[a], Hao Ling[a], and Victor C. Chen[b]

[a]Dept. of Electrical and Computer Engineering,
The Univ. of Texas at Austin, Austin, TX 78712-1084
[b]Airborne Branch, Naval Research Laboratory
Washington, DC 20375

ABSTRACT

In this paper, ISAR images generated from measured data are compared to those from computer simulation in order to evaluate the effectiveness of ISAR-based target identification. Three sets of images are generated including: (i) motion compensated images from measured data using a joint time-frequency technique, (ii) reference images from measured data and GPS-derived aircraft attitude data, and (iii) synthetic images predicted by Xpatch. Visual examination and correlation analysis are undertaken to compare the three sets of images. In addition, two problem areas including JEM line corruption of the measured images and three-dimensional rotation of the target are identified.

Keywords: inverse synthetic aperture radar (ISAR) imaging, motion compensation, joint time-frequency technique, Xpatch image prediction

1. INTRODUCTION

High-resolution inverse synthetic aperture radar (ISAR) imaging has been regarded as a possible tool for target identification.[1, 2] There are two important components to an ISAR-based target ID system. The first component is the image formation algorithm in which the raw data collected from an imaging radar is processed and motion compensated to form a focused image of the unknown target. The second component is an image database of known targets populated by either actual measurements or computer simulation. The focused image from measurement is then matched against the image database in order to determine the unknown target type. The success of an ISAR-based target ID system is therefore critically dependent on the quality of these two basic building blocks. In this paper, we carry out a comparison of ISAR imageries generated from motion compensated measure data and those from computer-simulated synthetic signatures. Our objectives are to provide an assessment of the current capabilities and identify possible hurdles in ISAR-based target ID.[3]

For this purpose, three sets of images are generated. First, the motion compensated images are generated from radar measurement data of an airplane in flight. Motion compensation is carried out using a joint time-frequency technique that has been reported previously.[4] We shall refer to these images as the JTF-mocomp images. Second, a set of reference images is generated by using the aircraft motion data collected during the flight from on-board GPS sensors. Even though this data is available only from cooperative data collection and not in the real target ID scenario, it serves as the ground truth for evaluating the effectiveness of the mocomp algorithm. We shall refer to these images as the GPS-reference images. Third, synthetic images are simulated from a CAD model of the aircraft using the electromagnetic signature prediction code Xpatch.[5] We shall refer to these images as the Xpatch-synthetic images.

This paper is organized as follows. In Section 2, the detailed methods are given on generating the JTF-mocomp, the GPS-reference and the Xpatch-synthetic ISAR images. Results are presented showing example images and the correlation between the three sets of images. From the correlation coefficients, two problem areas are identified. In Section 3, we examine the jet engine modulation (JEM) line issue in the frontal look region of the target and propose an algorithm to remove the JEM lines

---

[*] correspondence: Email:fei@ece.utexas.edu

from the measured images. In Section 4, we examine the variable imaging plane problem during certain portions of the flight. Conclusions are given in Section 5.

2. MEASURED AND SYNTHETIC IMAGE GENERATION

With the radar I/Q data, the tracking data, the GPS data and the CAD model of the aircraft, measured and simulated 2-D ISAR images can be generated. We first describe the procedures used to generate the JTF-mocomp, the GPS-reference and the Xpatch-synthetic ISAR images. From these results, we next carry out a comparison to evaluate the effectiveness of the motion compensation algorithm and the electromagnetic modeling.

2.1. Motion Compensation Using Joint Time-Frequency Algorithm

In the usual case of ISAR imaging where the complex target motion is not known, motion compensation is needed to form a focused ISAR image. For this purpose, we use a previously developed adaptive JTF algorithm.[4] We assume that after the coarse range alignment, all the scatterers are located in their respective range cells. The radar backscattered signal as a function of dwell time t_D in a particular range cell can be written as

$$E(t_D) = \sum_{k=1}^{N} A_k \exp[-j\frac{4\pi f}{c}(R(t_D) + x_k \cos\theta(t_D) + y_k \sin\theta(t_D))] \tag{1}$$

where N_k is the number of point scatterers in that range cell, and A_k, x_k, y_k are respectively the scattering amplitude, down range position and cross range position of the kth point scatterer. $R(t_D)$ is the residual uncompensated translation displacement and $\theta(t_D)$ is the rotational displacement. The JTF technique used here is a search and projection procedure to represent phase behavior of the signal $E(t_D)$. To find the motion parameters, basis functions in the form of

$$h(t) = \exp[-j2\pi(f_0 t + \frac{1}{2}f_1 t^2 + \frac{1}{3}f_2 t^3)] \tag{2}$$

are chosen. We search for the basis function over the parameter space (f_0, f_1, f_2) that best represents the time-frequency behavior of the signal by maximizing the projection of the signal onto the basis:

$$\max_{f_0, f_1, f_2} \left| \int E(t) h^*(t) dt \right|^2 \tag{3}$$

After the time-varying phase for the strongest point scatterer is found, we multiply the original signal by the conjugate of this phase factor to compensate for the translation motion. This algorithm can also be extended to multiple range cells to correct for higher order rotation motion. Figs. 1 and 2 show the JTF processing concept. After coarse range alignment, a particular range bin may contain multiple scatterers with time-varying Doppler frequencies. The (dwell time)-(Doppler frequency) behaviors of these scatterers are illustrated in Fig. 1(b). Fig. 2(a) shows the JTF behavior of a dominant scatterer in a range cell from actual measurement data. We see from Fig. 2(b) that after the JTF compensation, its trajectory is straightened. After applying the JTF motion compensation, the standard FFT processing in the dwell time domain brings the signal into the cross range image domain.

2.2. Ground Truth Image Generation Using GPS Data

The motion parameters from on-board GPS sensors collected during the cooperative flight of the airplane are next used to generate the ground truth ISAR images. The resulting reference images can be used to evaluate the quality of the JTF-mocomp images from the last section. Furthermore, the motion data can be used to extract azimuth and elevation look angle information for carrying out the electromagnetic simulation of the aircraft.

First, coordinate transformation is carried out since the GPS data is in the fixed Earth system, while the desired azimuth and elevation angles are defined with respect to the local coordinate of the aircraft (see Fig. 3). The latter information is needed for the simulation process and for determining the absolute scaling of the measured images along the cross range dimension. Unlike the JTF motion compensation where the coarse range alignment is carried out based on range profile correlation, here range data from the GPS measurement are used directly for range alignment. In addition, the aspect angle versus dwell time

information is used to correct for higher-order rotational motions. We reformat the data from uniform sampling in dwell time to uniform sampling in aspect angle. The FFT is then used to generate the final ISAR images. Since the look angle information is available, the resulting ISAR images can be scaled in the cross range dimension to absolute physical size.

2.3. Synthetic Signature Prediction Using Xpatch

To test the effectiveness of electromagnetic modeling for ISAR imaging, we generate the simulated ISAR images using Xpatch and the radar and aircraft motion parameters from Section 2.2. Xpatch is an electromagnetic computation code based on the shooting and bouncing ray method.[6] It can be used to compute the backscattering of complex targets of large electrical sizes. In the Xpatch simulation, rays are shot from the incident look angle and all the multiple reflections are tracked until the rays exit the target (see Fig. 4). The image is simulated by updating the ISAR image plane one ray at a time using its ray-spread function.[7] The image update is further accelerated by an FFT-based algorithm.[8] Note that this fast image simulation algorithm requires only a single ray trace per image. It is therefore orders of magnitude faster than the conventional method that requires multi-frequency, multi-aspect data. The typical simulation time using this approach is approximately 30 minutes per image on an SGI O2 workstation.

While the ISAR images generated from Xpatch contain absolute scaling along the cross range dimension, the ISAR images from the JTF-mocomp process is not calibrated along that dimension since the rotational speed is not known. Here we take advantage of the look angle information derived from the GPS data. Prior to making any image comparisons, we first re-scale the Xpatch images such that they have the same cross range resolution and scaling as the images from the measured data.

2.4. Image Comparisons

In this section, we make image comparisons among the three sets of ISAR images: the JTF-mocomp images, the GPS-reference images and the Xpatch-synthetic images. Fig. 5 shows one set of such comparisons. The look angle is near tail-on of the airplane. The JTF-mocomp image is shown in Fig. 5(a). It is fairly well focused and the features from the tail, the two wings and the fuselage are clearly exposed. The GPS-reference image is shown in Fig. 5(b). We observe that the agreement between the JTF-mocomp and the GPS-reference images is good. Fig. 5(c) shows the corresponding Xpatch-synthetic image. Again the outline of the aircraft is readily observed in this image, although the image is much more focused than the two images from measured data. Our experience shows that the JTF motion compensation works well during most of the fight time. After a side-by-side visual examination, we find that most mocomp images are in fact slightly better focused than the reference images. We believe this is due to the limited accuracy of the GPS sensor data. The synthetic images show good qualitative agreement with the measured images. However, they are in general less diffused than the measured images. This is not surprising since the synthetic image formation assumes no motion errors. Furthermore, the CAD model used does not capture all of the fine details of the actual target.

While the comparison from visual examination shows promising agreement between the three sets of images, an image correlation is undertaken for a more quantitative comparison. Before the correlation, the images are power transformed to account for the different dynamic ranges. Fig. 6 shows both the correlation coefficient between the JTF and GPS images, and that between the JTF and Xpatch images versus azimuth look angle. From the two curves, we see that the JTF-mocomp images agree very well with its GPS-reference counterparts, indicating that blind motion compensation is a very feasible method for processing real-world radar data. The correlation coefficient between the JTF and Xpatch images is in general lower than that between the measured images. In particular, two problem regions can be seen from this plot. First, in the region near nose-on (180 degrees in azimuth), the correlation coefficient is significantly lower. The reason is due to JEM lines in the measured data. This problem is further discussed in Section 3 and an algorithm to remove JEM lines is proposed. Second, at some angles around the broadside region (90 degrees in azimuth), the correlation coefficient is also low. The associated JTF images are found to be of low quality. After further investigation, it is found that the image blurring is due to variations in the imaging plane, not the motion compensation processing. This problem is discussed in detail in Section 4.

3. JEM REMOVAL

Jet engine modulation is a phenomenon caused by the high-speed rotational movement of the aircraft engine.[9, 10] For an imaging radar, the typical PRF is much slower than the engine rotation frequency. Thus the resulting ISAR image in the frontal region of an aircraft contains an aliased component along the cross range dimension. Such effect is difficult to predict accurately using simulation. Furthermore, JEM lines are noise-like and can corrupt the geometrical features of the target in

the ISAR image. For target ID using 2D ISAR imaging, it would be useful to devise an algorithm to remove JEM lines, and therefore enhance the image and the subsequent ID process.

Let us assume that the aircraft consists of a slow moving body with a constant rotational velocity Ω_b and a fast moving engine component with a different rotational velocity Ω_p. Then the received radar return as a function of dwell time can be written as:

$$E(t_D) = \sum_{k=1}^{N_b} A_k \exp[-j\frac{4\pi f}{c}(R(t_D) + x_k \cos(\Omega_b t_D) + y_k \sin(\Omega_b t_D)]$$
$$+ \sum_{k=N_b+1}^{N} A_k \exp[-j\frac{4\pi f}{c}(R(t_D) + x_k \cos(\Omega_p t_D) + y_k \sin(\Omega_p t_D)]$$

(4)

where N is the total number of point scatterers within one range cell, of which N_b are the body scatterers. Usually Ω_p is much greater than Ω_b. While the first term can be meaningfully mapped into the image plane of the target via the Fourier transform, the second term results in serious Doppler smearing across the cross range domain and may overshadow the target features.

We can also utilize the joint time-frequency technique described earlier under motion compensation to separate the fast moving part from the relatively slow moving body.[11] For the component due to target body scattering, the Doppler frequency is

$$f_D^b = \frac{4\pi f}{c}\Omega_b[y\cos(\Omega_b t_D) + x\sin(\Omega_b t_D)] \approx \frac{4\pi f}{c}\Omega_b(y + x\Omega_b t_D)$$

(5)

while the Doppler frequency due to the fast rotating part is

$$f_D^p = \frac{4\pi f}{c}\Omega_p[y\cos(\Omega_p t_D) + x\sin(\Omega_p t_D)]$$

(6)

We can see that (5) is a linear function of dwell time while (6) is a sinusoidal function. In the time-frequency plane, the two signals can thus be distinguished. If we further parameterize the signal by basis functions that have linear Doppler frequency behavior as a function of dwell time, the two signals can be separated automatically by their displacement and slope parameters. We utilize the adaptive joint time-frequency processing technique to carry out the parameterization. The basis used is similar to that given in (2) with the linear and quadratic phase terms. The project and search procedure given in (3) is carried out iteratively. At each iteration, the basis parameters (f_0, f_1) and B_p, which is the maximum projection value of the signal onto the basis, are found. The best basis at stage p is then removed from the signal:

$$E_{p+1}(t) = E_p(t) - B_p h_p(t)$$

(7)

The searching process is iterated until the energy of the residue signal is smaller than a preset threshold. The signal component due to the target scattering can thus be reconstructed by using all the bases with small displacement f_0 and small slope parameter f_1. Fig. 7 shows the correlation between the synthetic images and the measure images after JEM removal. We observe that the correlation coefficients in the JEM region are increased after we remove the JEM interference from the body.

4. IMAGING PLANE VARIATION

From the correlation curves, some images generated from the measured data outside of the JEM angular region are also found to be poorly focused. For those frames, we have found that the associated GPS-reference images also fail. If we assume the data quality from the radar did not change abruptly, the cause must not be in the motion compensation algorithm, but rather from extraneous motions during the imaging interval, which cannot be handled by any motion compensation method. Here we examine the possible causes. The movement of the aircraft in space relative to the ground radar consists of radial motion and rotational motion. Because the range alignment process can remove the radial motion, what remains a problem is the 3D rotational motion of the aircraft. Suppose during the imaging interval the rotational motion is described by the look angles (θ, ϕ) on the target. The requirement of a constant rotation axis described by (θ_0, ϕ_0) leads to the following equation that constraints the values of (θ, ϕ):

$$\sin\theta_0 \sin\theta \cos(\phi - \phi_0) + \cos\theta_0 \cos\theta = 0 \qquad (8)$$

If $\theta_0=0$, eq. (8) requires $\theta=\pi/2$. In this case, the aircraft rotates about its vertical axis and the imaging plane is the top view of the airplane. If $\theta_0=\pi/2$ and $\phi_0=\pi/2$, then $\phi=0$. In this case, the aircraft rotates about its axis along the wing and the imaging plane is the side view of the airplane.

The images from these two cases will be quite different. If an imaging interval includes both types of motion, the resulting image is expected to be unfocused. Although this is an extreme example, we do observe several cases in the real data where the imaging plane variation in the 128 pulse records leads to bad images. Fig. 8 shows a particular example of imaging plane variation. From the azimuth-elevation plot in Fig. 8(a) derived from the GPS data, we recognize two different imaging planes. During the first half of the 128 records, the aircraft undertakes nearly a vertical rotation, while during the second part it undertakes a horizontal rotation. So we get a very smeared image as shown in Fig. 8(b). We can get a better image by using only the first part or the second part of the data. The resulting image from the first part of the data is a side view of the aircraft, while the image from the second part of the data is a top view of the aircraft. Unfortunately, we usually do not have access to the aircraft attitude data on non-cooperative targets. In such cases, the questions of how to detect imaging plane variation and how to form the best possible images become important research issues. This topic is currently under investigation by us.

5. CONCLUSIONS

To evaluate the effectiveness of ISAR-based target ID, ISAR images generated from measured data are compared to those from computer simulation. Three sets of images are generated including: (i) motion compensated images from measured data using a joint time-frequency technique, (ii) reference images from measured data and GPS-derived aircraft attitude data, and (iii) synthetic images predicted by Xpatch. Visual examination and correlation analysis are undertaken to compare the three sets of images. Through the comparisons, the following conclusions can be made. First, JTF motion compensation method performed well with real world ISAR data. Second, Xpatch is a feasible tool to generate a synthetic image database for ISAR-based target ID. Two problem areas are also identified. JEM line corruption of the measured images is quite severe in the frontal sector of air targets. A possible algorithm based on joint time-frequency technique is proposed to remove the JEM lines. In addition, the problem of imaging plane variation is identified to be the cause of poor ISAR images during some time of the flight. Further investigation is needed to devise methods to overcome this problem.

ACKNOWLEDGEMENT

REFERENCES

1. C. C. Chen and H. C. Andrews, "Target motion induced radar imaging," *IEEE Trans. Aerospace Electron. Syst.*, vol. 16, pp.2-14, Jan. 1980.
2. A. Ausherman, A. Kozma, J. L. Waker, H.M. Jones and E. C. Poggio, "Developments in radar imaging," *IEEE Trans. Aerospace Electron. Syst.* vol. 20, pp.363-400, Apr. 1984.
3. H. Ling, Y. Wang, J. Li, R. Bhalla and V.C. Chen, "ISAR image formation of TIRA data using adaptive joint time-frequency processing," *NATO Sensors and Electronics Technology Symposium on High Resolution Radar Techniques*, Granada, Spain, Mar. 1999.
4. Y. Wang, H. Ling and V. C. Chen, "ISAR motion compensation via adaptive joint time-frequency technique," *IEEE Trans. Aerospace Electron. Syst.*, vol. 34, pp.670-677, Apr. 1998.
5. D. J. Andersh, M. Hazlett, S. W. Lee, D. D. Reeves, D. P. Sullivan and Y. Chu, "XPATCH: a high-frequency electromagnetic-scattering prediction code and environment for complex three-dimensional objects," *IEEE Antennas Propagat. Mag.*, vol.36, pp.65-69, Feb. 1994.
6. H. Ling, R. Chou and S.W. Lee, "Shooting and bouncing rays: Calculating the RCS of an arbitrary shaped cavity," *IEEE Trans. Antennas Propagat.*, vol. 37, pp.194-205, Feb. 1989.

7. R. Bhalla and H. Ling, "Image-domain ray-tube integration formula for the shooting and bouncing ray technique," *Radio Science*, vol. 30, pp.1435-1446, Sept.-Oct. 1995.

8. R. Bhalla and H. Ling, "A fast algorithm for signature prediction and image formation using the shooting and bouncing ray technique," *IEEE Trans. Antennas Propagat.*, vol. AP-43, pp.727-731, July 1995.

9. F. E. Nathanson, *Radar Design Principles*, pp.173-183, McGraw-Hill, New York, 1969.

10. M. Bell and R. A. Grubbs, "JEM modeling and measurement for radar target identification," *IEEE Trans. Aerospace. Electron. Syst.*, vol. 29, pp. 73-87, 1993.

11. Y. Wang, H. Ling and V.C. Chen, "Application of adaptive joint time-frequency processing to ISAR image enhancement and Doppler feature extraction for targets with rotating parts," *SPIE 43rd Annual Meeting, Radar Processing, Technology, and Applications*, pp. 156-163, San Diego, CA, July 1998.
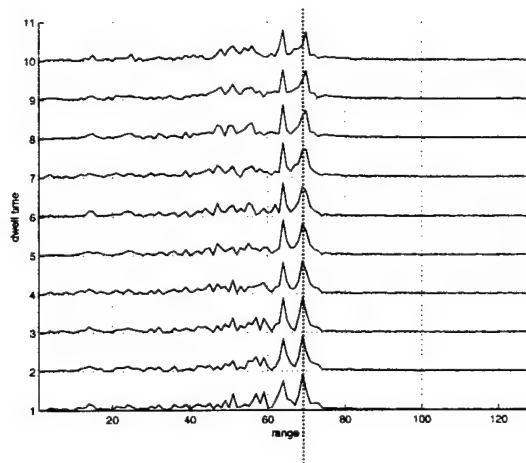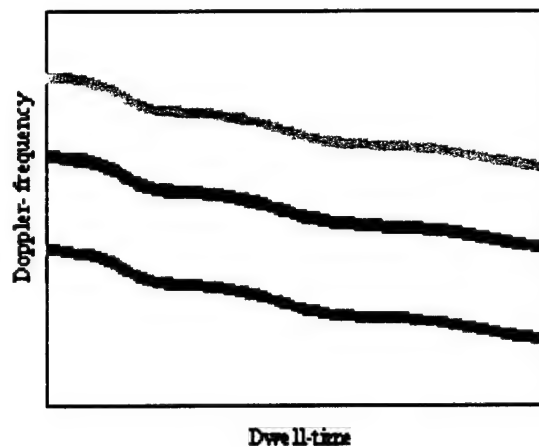
Fig. 1.   Fine motion compensation is carried out by extracting
the Doppler frequency versus dwell time behavior of
the strong point scatterer in the signal.
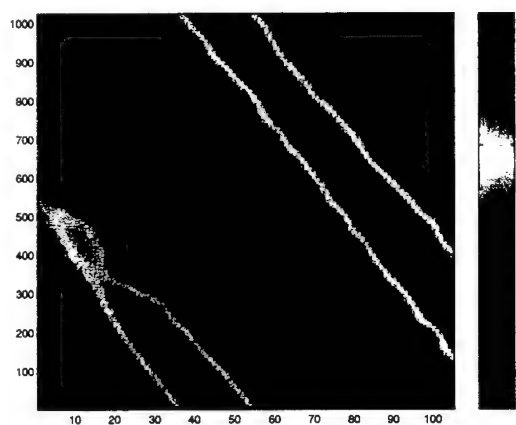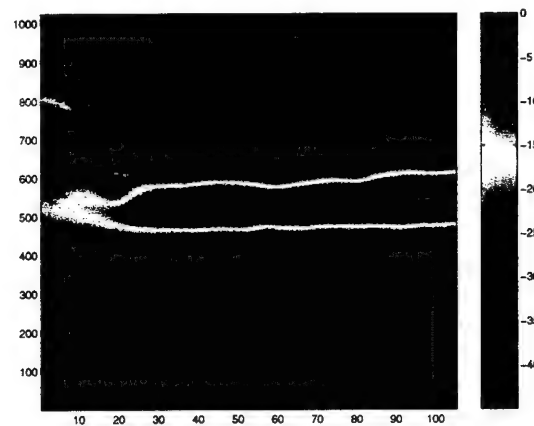
Fig. 2.   Trajectory of a strong scatterer in the (dwell time)-
(Doppler-frequency) plane from measured data.
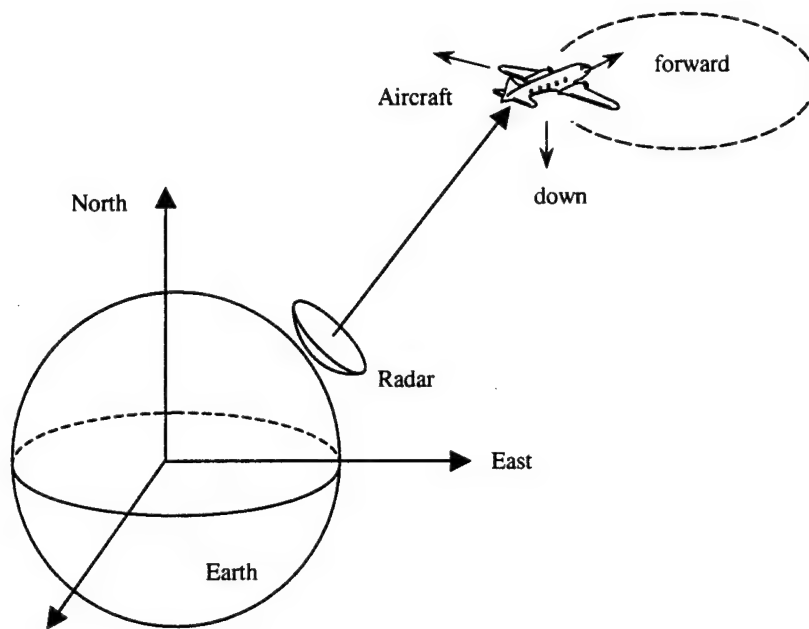(a) Before JTF motion compensation.
(b) After JTF motion compensation.

Fig. 3.   Global and local coordination systems of the
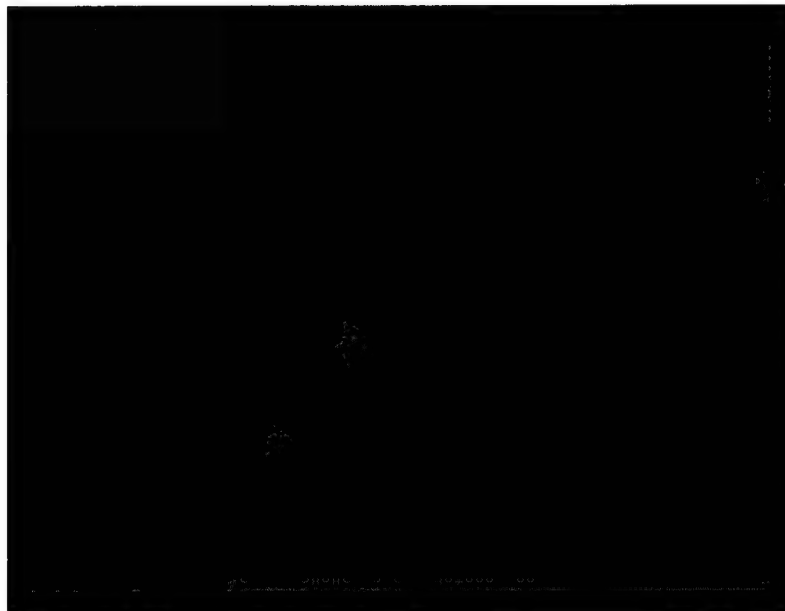problem (figures not drawn to scale).

Fig. 4.   Shooting and bouncing ray technique for radar
signature simulation.
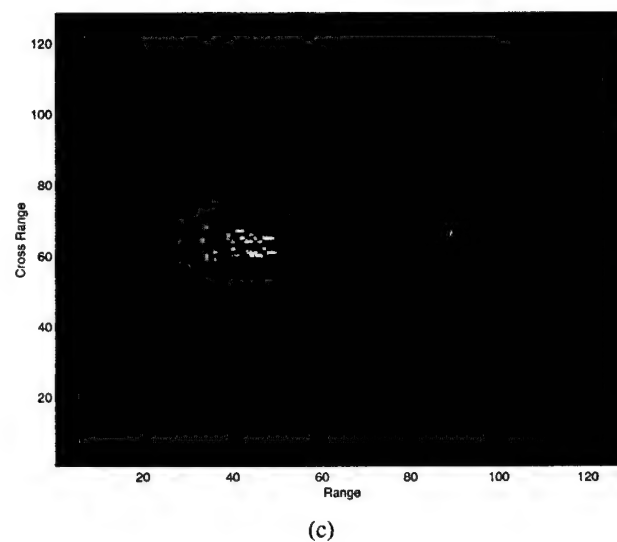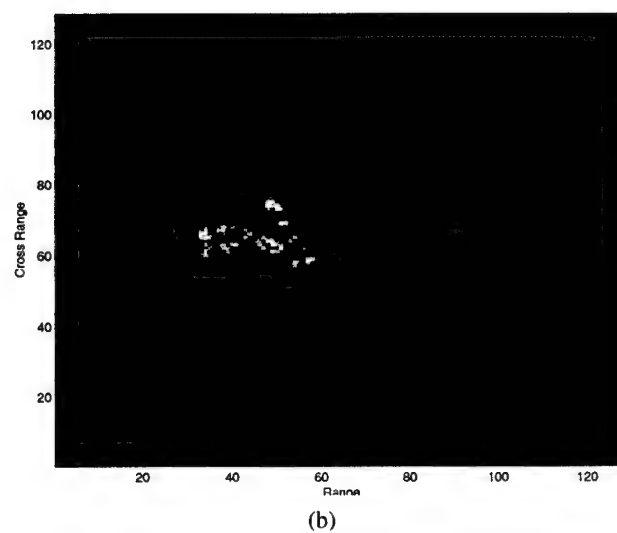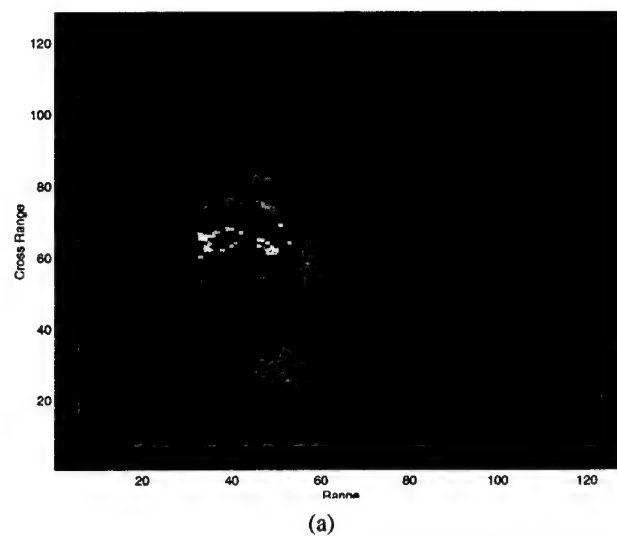
Fig. 5. ISAR images from: (a) JTF-mocomp, (b) GPS-reference, and (c) Xpatch-synthetic.
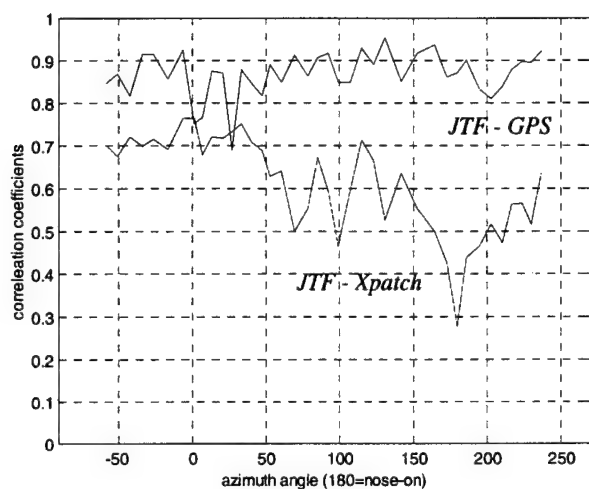
Fig. 6.   Correlation coefficients between JTF and GPS images, and between JTP and Xpatch images.
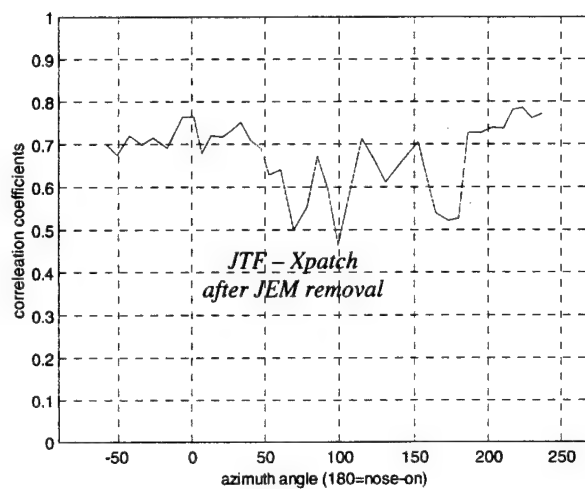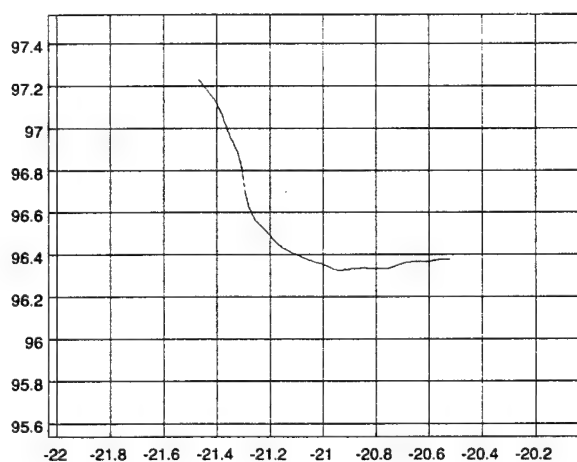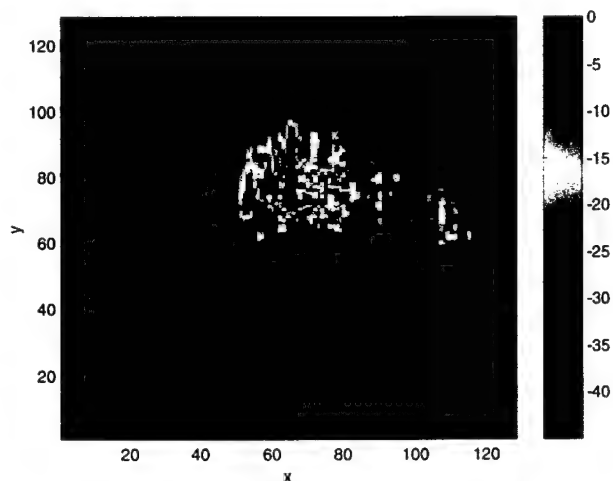
Fig. 7.   Correlation between JTF and Xpatch images after JEM removal.

(a)

(b)

Fig. 8. Effect of imaging plane variation on ISAR image.

Application of Adaptive Joint Time-Frequency Processing to ISAR Image Formation

Hao Ling and Junfei Li
Dept. of Electrical and Computer Engineering
The Univ. of Texas at Austin
Austin, TX 78712-1084

I. Introduction

High-resolution inverse synthetic aperture radar (ISAR) imaging is a promising tool for non-cooperative target identification (NCTI). The main challenge in ISAR-based NCTI is to form a well-focused image of an articulating target with unknown motion. In this paper, we first review the application of joint time-frequency methods for ISAR image formation. By using an adaptive joint time-frequency (AJTF) algorithm to estimate the phase of the prominent scatterers, we show that the target motion can be estimated and a focused image of the target can be constructed. Results of applying the algorithm to measured ISAR data are presented and discussed. Secondly, we report on our recent work to extend the AJTF algorithm to address the more challenging situation when the motion of the target is not limited to a two-dimensional plane. In particular, we discuss our research to: (i) detect the presence of three-dimensional motion using the AJTF algorithm, and (ii) develop algorithms to focus the image in the presence of complex three-dimensional motion.

2. ISAR Motion Compensation Using Joint Time-Frequency Algorithm

We first review the application of joint time-frequency methods for ISAR image formation. To form a focused image from raw radar data, it is customary to first carry out a coarse alignment of the data in the range dimension, followed by fine motion compensation in the cross range dimension. Joint time-frequency techniques have been shown to be a useful tool to carry out the fine motion compensation [1,2]. We assume that after the coarse range alignment, all the scatterers are located in their respective range cells. The radar backscattered signal as a function of dwell time t in a particular range cell can be written as

$$E(t) = \sum_{k=1}^{N} A_k \exp[-j\frac{4\pi f}{c}(R(t) + x_k \cos\theta(t) + y_k \sin\theta(t))] \tag{1}$$

where N is the number of point scatterers in that range cell, and A_k, x_k, y_k are respectively the scattering amplitude, down range position and cross range position of the kth point scatterer. $R(t)$ is the residual uncompensated translation displacement and $\theta(t)$ is the rotational displacement. Due to translation and rotational motion, the Doppler frequency versus dwell time behavior of the point scatterers within this range cell is not constant in the joint time-frequency plane (see Fig. 1). An effective JTF technique to extract the motion parameters is based on a search and projection procedure to represent the phase behavior of the signal $E(t)$. This procedure is based on the adaptive spectrogram proposed in [3], and is similar in concept to a one-term matching pursuit algorithm [4]. We shall term it the adaptive JTF (AJTF) algorithm. To find the motion parameters, basis functions in the form of

$$h(t) = \exp[-j(a_1 t + a_2 t^2 + a_3 t^3)] \tag{2}$$

are chosen. We search for the basis function over the parameter space (a_1, a_2, a_3) that best represents the time-frequency behavior of the signal by maximizing the projection of the signal onto the basis:

$$\max_{a_1, a_2, a_3} \left| \int E(t) h^*(t) dt \right|^2 \tag{3}$$

After the time-varying phase for the strongest point scatterer is found, we multiply the original signal by the conjugate of this phase factor to compensate for the translation motion. This algorithm can also be extended to multiple range cells to correct for higher order rotation motion. After applying the JTF motion compensation, the standard FFT processing in the dwell time domain brings the signal into the cross range image domain. Results of applying the algorithm to simulated and measured ISAR data will be presented and discussed.
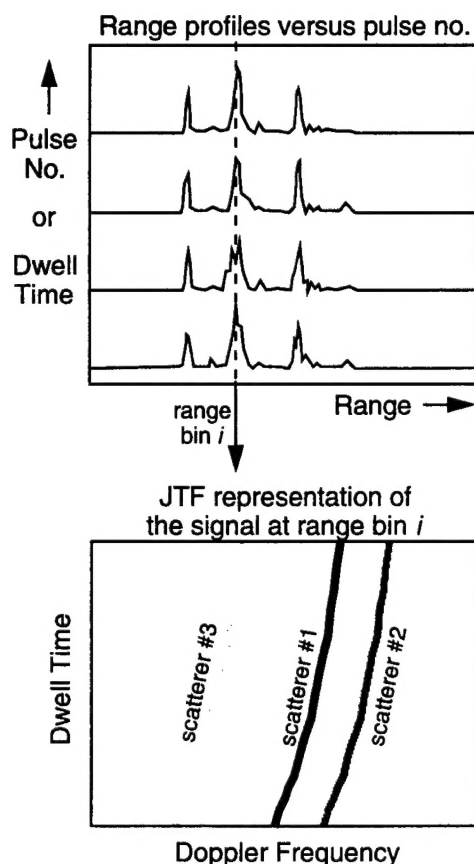

Fig. 1. Fine motion compensation is carried out by extracting
the Doppler frequency versus dwell time behavior of
the strong point scatterer in the signal.

3. Three-Dimensional Motion Estimation Using Joint Time-Frequency Algorithm

One basic assumption of standard motion compensation algorithms is that the target only undergoes motion in a two-dimensional plane during the dwell duration needed to form an image. From several independent examinations of measured ISAR data sets recently, it was reported that the presence of three-dimensional motion is quite detrimental to focusing the image [5-7]. We shall report on our recent work to extend the AJTF algorithm to address the more challenging situation when the motion of the target is not limited to a two-dimensional plane. In particular, we discuss our research to: (i) detect the presence of three-dimensional motion using the AJTF algorithm, and (ii) develop algorithms to focus the image in the presence of complex three-dimensional motion.
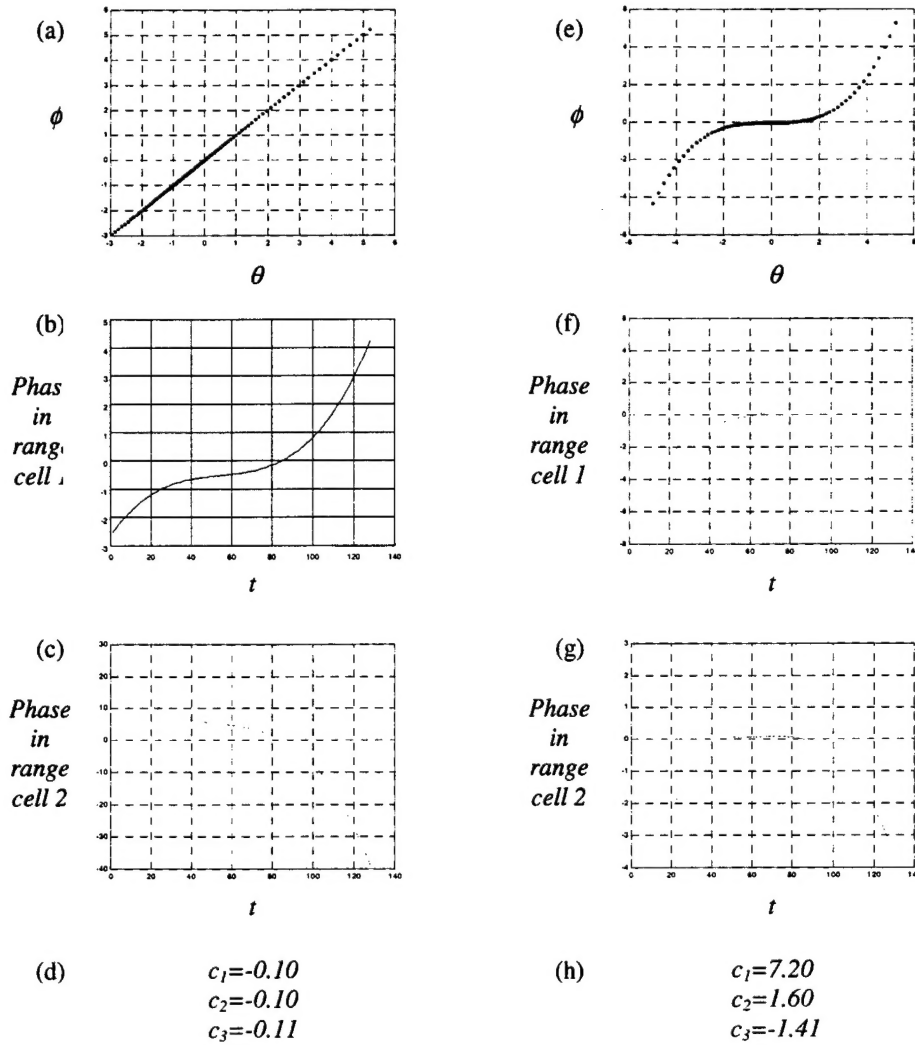
Fig. 2. (a) Simulated 2D target motion. (b) Phase behavior of the prominent point scatterer in range cell 1 extracted using AJTF. (c) Phase behavior of the prominent point scatterer in range cell 2 extracted using AJTF. (d) Ratios of the extracted phase parameters from the two range cells. Note that they are nearly constant. (e)-(h) Similar to (a)-(d), except that 3D motion is assumed. The resulting ratios in (h) are no longer constant.

Allowing for arbitrary three-dimensional motion in space, we consider the following model as a generalization of the model for two-dimensional motion in (1):

$$E(t) = \sum_{k=1}^{N} A_k \; exp[-j \frac{4\pi f_c}{c}(x_k + y_k \theta + z_k \phi)]$$ (4)

where θ is the azimuth angle of the target with respect to the radar, and ϕ is the elevation angle. In (4), it is assumed that the translation motion has been removed and that the standard small-angle, small bandwidth

approximations apply. This model reduces to the standard two-dimensional motion model when θ and ϕ are linearly related.

In general, a focused image cannot be obtained from the standard two-dimensional motion compensation algorithm when three-dimensional target motion is present due to model mismatch. Therefore, it would be useful to detect the presence of three-dimensional motion directly from the radar data. Our approach is to utilize the AJTF algorithm to extract the phase behavior of the radar data at multiple range cells. We first parameterize the phase of the prominent point scatter in one range cell using AJTF. Next we repeat the same procedure at another range cell. It can be shown that when the target undergoes only two-dimensional motion during the dwell duration, the ratio between the parameters (a_1, a_2, a_3) extracted from one range cell and those corresponding parameters in another range cell should be constant. Therefore, by examining the ratio of the parameters, we can distinguish two-dimensional motion from three-dimensional motion. Fig. 2 illustrates the idea using simulated point scatterer data. Figs. 2(a)-(d) show the two-dimensional motion scenario and Figs. 2(e)-(h) show the three-dimensional scenario. It can be seen from the results in Fig. 2(d) that the determined ratios:

$$c_i = a_i(\text{range cell 1}) \, / \, a_i(\text{range cell 2}) \tag{5}$$

are nearly constant for all the terms in case of two-dimensional motion, as expected. For three-dimensional motion, the ratios are not the same, as seen in Fig. 2(h). Results of applying this concept to radar data in order to isolate the time durations when the target undergoes three-dimensional motion will be presented.

REFERENCES

1. V. C. Chen, "Reconstruction of inverse synthetic aperture images using adaptive time-frequency wavelet transforms," SPIE Proc. on Wavelet Application, vol. 2491, pp. 373-386, 1995.
2. Y. Wang, H. Ling and V. C. Chen, "ISAR motion compensation via adaptive joint time-frequency technique," *IEEE Trans. Aerospace Electron. Syst.*, vol. 34, pp.670-677, Apr. 1998.
3. S. Qian and D. Chen, "Signal representation using adaptive normalized Gaussian functions," *Signal Processing*, vol. 36, no. 1, pp. 1-11, Mar. 1994.
4. S. G. Mallat and Z. Zhang, "Matching pursuits with time-frequency dictionaries," *IEEE Trans. Signal Processing*, vol. 41, pp. 3397-3415, Dec. 1993.
5. V.C. Chen and W. J. Miceli, "Effect of roll, pitch and yaw motions on ISAR imaging," SPIE Proc. on Radar Processing, vol. 3810, July 1999.
6. A. W. Rihaczek and S. J. Hershkowitz, "Choosing imaging intervals for identification of small ships," SPIE Proc. on Radar Processing, vol. 3810, July 1999.
7. J. Li, Y. Wang, R. Bhalla, H. Ling and V. C. Chen, "Comparison of high-resolution ISAR imagery from measured data and synthetic signatures," SPIE Proc. on Radar Processing, vol. 3810, July 1999.